

### UNIVERSITÀ DEGLI STUDI DI MILANO

Facoltà di Scienze e Tecnologie Laurea Triennale in Fisica

# A Study of Copper Adatom Binding on Carbon Nanotubes via Density Functional Theory

Relatore: Prof. Francesca Baletto Co-relatore: Prof. Nicola Manini

> Riccardo Piazza Matricola nº 986226 A.A. 2024/2025

# A Study of Copper Adatom Binding on Carbon Nanotubes via Density Functional Theory

Riccardo Piazza

Dipartimento di Fisica, Universitá degli Studi di Milano,

Via Celoria 16, 20133 Milano, Italia

October 29, 2025

#### Abstract

The objective of this thesis is to study the adsorption properties of copper atoms on a single-walled zigzag (12,0) carbon nanotube. The Cu/CNT system is a subject of numerous studies for catalysts purpouse and it's mechanical and electronic peculiar characteristics.

Ab initio calculations based on Density Functional Theory (DFT), implemented in the *Quantum ESPRESSO* package, were performed to investigate the adsorption sites and their corresponding adsorption energies  $E_{\rm ads}$ .

The results indicate that the Cu adatom preferentially adsorbs on the outer surface of the CNT, specifically at the axial bridge site. The external binding energy is found to be between 0.3 and 0.6 eV, a value characteristic of physisorption. Internal adsorption is found to be energetically less favorable, with very low binding energies ( $\sim 0.13$  eV). This demonstrates that the CNT curvature plays a significant role in determining the adsorption strength and sites stability.

# Contents

1	roduction	3				
	1.1	Carbon nanotubes	4			
	1.2	Metal adsorption on graphene and nanotubes	7			
2	Met	Methodology				
	2.1	The DFT scheme	10			
		2.1.1 The Born-Oppenheimer approximation	10			
		2.1.2 The Hohenberg-Kohn theorems	11			
		2.1.3 The Kohn-Sham equations	12			
		2.1.4 Solution to the Kohn-Sham equations	14			
		2.1.5 Precision and accuracy of DFT	16			
		2.1.6 Numerical parameters	17			
	2.2	The QuantumESPRESSO package	18			
		2.2.1 The pw.x input file	19			
		2.2.2 The pw.x output file	20			
3	Set	up	<b>2</b> 5			
	3.1	The atomic configuration				
	3.2	Setting up the calculations	26			
		3.2.1 Convergence tests	26			
		3.2.2 Energy cutoff	26			
		3.2.3 Cell size	27			
		3.2.4 <b>k</b> -point sampling	28			
		3.2.5 Smearing	29			
	3.3	CNT structural relaxation	30			
4	Cha	aracterizing the Cu/CNT system	32			
_		External adsorption	33			

	4.2	Internal adsorption					
	4.3	4.3 Structural analysis					
		4.3.1	Total atomic displacement	36			
		4.3.2	Radial deformation	37			
		4.3.3	Stress tensor	38			
	4.4	Electr	onic structure and charge analysis	39			
		4.4.1	Electronic bands	39			
		4.4.2	Bader's charge analysis	40			
		4.4.3	Discussion	41			
	4.5	Concl	usion	43			
$\mathbf{A}$	CN	T conf	iguration generator	44			

## Chapter 1

## Introduction

Metal atoms anchored to functionalized carbon allotropes, see Fig. 1.1, play a versatile role in nanotechnology and materials science. They can be engineered to act as sensitive probes for detecting small molecule adsorption, making them useful in chemical sensing applications. These systems also contribute to hydrogen storage by enhancing sorption capacity and stability, and serve as active sites for catalytic reactions, improving efficiency and selectivity in various chemical processes. Additionally, they facilitate the controlled growth of metallic nanowires and support the development of nanoscale electronic devices by enabling precise fabrication techniques. In particular, copper adatoms and Cu-clusters on carbon nanotubes (Cu/CNTs) are promising candidates for lightweight, high-performance applications in electronics, aerospace, and energy systems, as they combine copper's excellent conductivity with the exceptional strength and stability of CNTs.

The aim of this thesis is to study the adsorption properties of copper atom(s) onto a single-walled CNT, in particular a zigzag (12,0). We perform ab initio Density Functional Theory (DFT) calculations to investigate adsorption sites and evaluate the corresponding binding energies. Our results show that a single Cu atom preferentially adsorbs on the external surface of the CNT, with a binding energy of  $\sim 0.3$ -0.6 eV, while internal adsorption is energetically less favorable with  $\sim 0.1$  eV binding energies. This indicates that curvature plays a significant role in determining the adsorption strength and site preference.

This thesis is organized as follow:

- Chapter 1: introduction to CNT and graphene properties and applications.
- Chapter 2: theoretical framework of the DFT and presentation of *QuantumESPRESSO* package.
- Chapter 3: system setup and simulation parameters convergency tests.

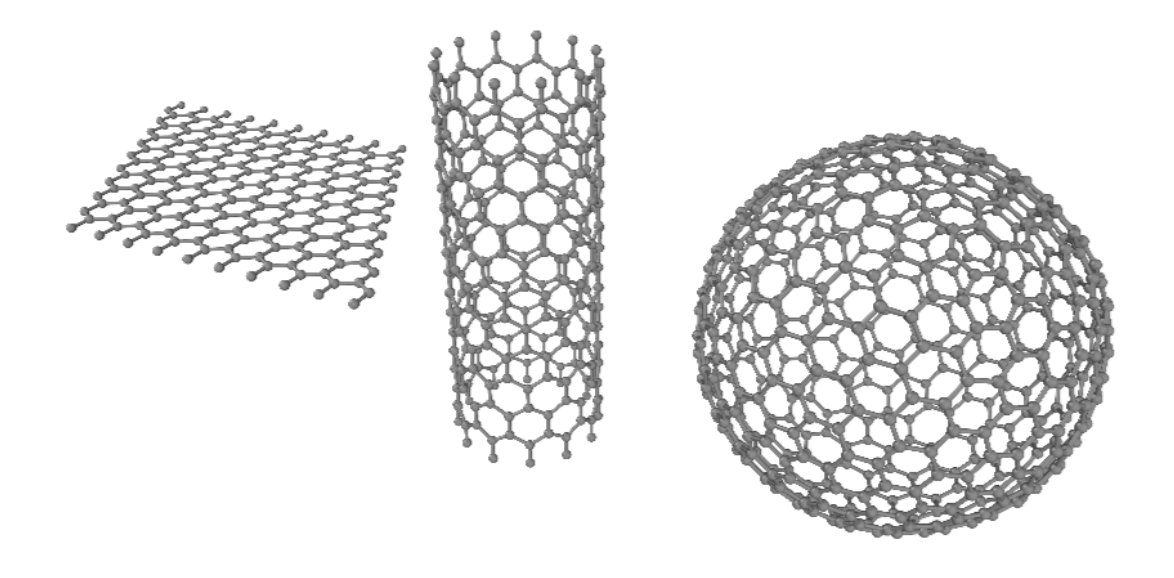


Figure 1.1: Left to right: a graphene sheet, a zigzag carbon nanotube, and a  $C_{540}$  fullerene. Those are examples of carbon allotropes based on  $sp^2$  hybridization.

• Chapter 4: calculations and analysis of results, including a comparison with literature data.

My thesis investigates whether a zigzag (12,0) CNT can accommodate a Cu atom inside the tube. We also analyze how curvature affects Cu adsorption, comparing our results with literature data for (8,0) CNTs and graphene layers.

#### 1.1 Carbon nanotubes

Carbon nanotubes (CNTs) are carbon allotropes with a quasi-one dimensional cylindrical structure, see Fig. 1.2, derived from rolled graphene sheets. They are classified in two categories: single and multi-walled CNT.

The synthesis of fullerenes via arc-discharge generated interest in discovering new graphenic nanostructures. Multi-walled nanotubes (MWCNTs) are multiple concentric graphene cylinders, the first being discovered in 1991 by Iijima [11] with a similar apparatus and analyzed with electron microscopy.

Single-walled CNTs (SWCNTs, in the following thesis sections simply CNTs) were synthetised for the first time in 1993 by Iijima and Ichihashi [12] and Bethune et al. [3] independently using transition-metal catalysts in arc-discharge pro-

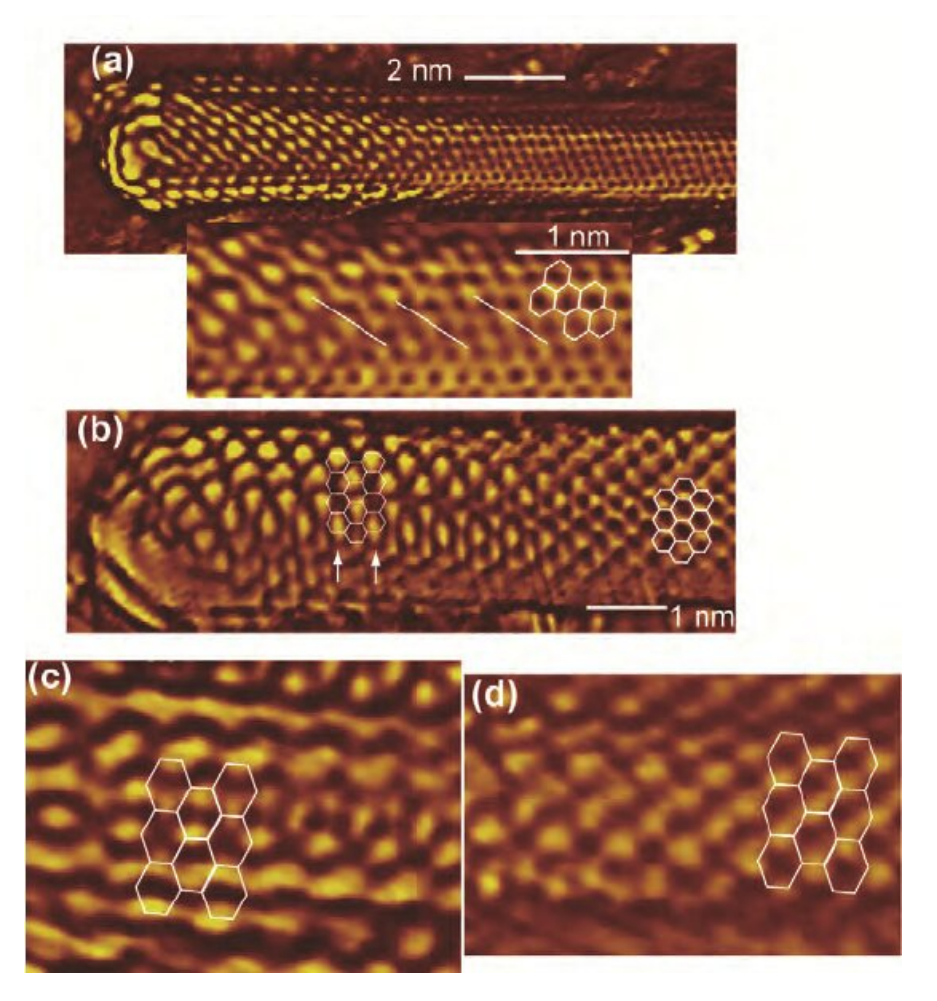


Figure 1.2: A few experimental Scanning Tunneling Microscope (STM) images of carbon nanotubes. From Ref. [15].

cesses, consisting of a single rolled graphene layer.

Since their discovery the community have conducted numerous studies because their unique properties. CNTs exhibit exceptional mechanical strength (Young's modulus ~1 TPa), high thermal conductivity (~3000 W/m·K), and unique electronic properties, ranging from metallic to semiconducting behavior depending on chirality, described below, and diameter. These characteristics make CNTs an important object of studies in condensed matter, nanoelectronics and quantum technology research works.

The chirality is defined by the chiral vector

$$\mathbf{A} = n\mathbf{a}_1 + m\mathbf{a}_2 \tag{1.1}$$

where (n, m) are integers, often called chiral indices, and  $\mathbf{a_1}$  and  $\mathbf{a_2}$  are the primitive vectors of the graphene lattice. The chiral vector wraps around the nanotube

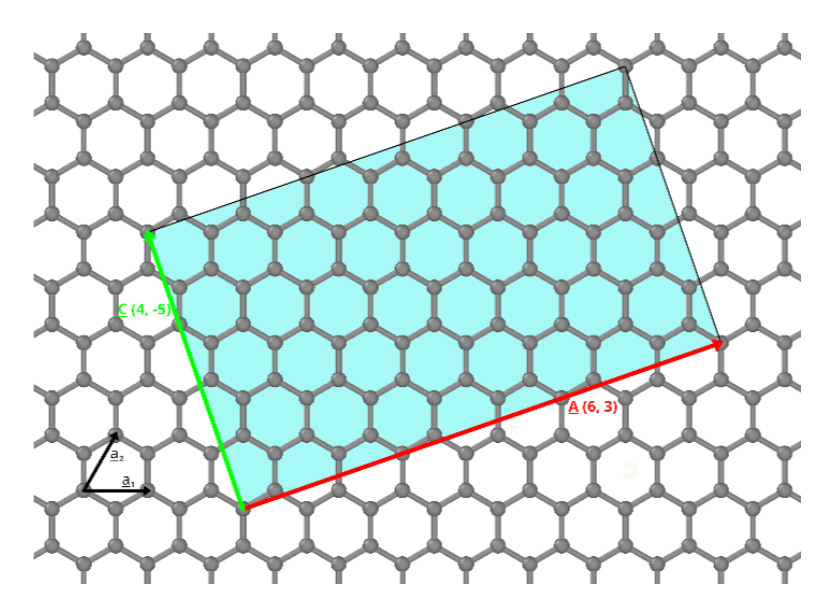


Figure 1.3: A graphene with  $\{\mathbf{a}_1, \mathbf{a}_2\}$  lattice vectors. The highlighted surface is the primary cell of a (6,3) CNT unwrapped, with the red chiral vector  $\mathbf{A}$  and the green translational vector  $\mathbf{C}$ .

and determines its circumference. Nanotubes with smaller diameters, that is, those with lower chiral indices, exhibit higher curvature. This curvature forces the local bonding geometry to deviate from the ideal planar sp<sup>2</sup> configuration, affecting the electronic structure and energy.

When approximated as an infinitely long tube, the CNT can be modeled as a one-dimensional crystal, whose unit cell corresponds to the minimal periodically repeated segment allowed by the chirality.

The radius R of a nanotube is given by

$$R = \frac{a}{2\pi} \sqrt{n^2 + nm + m^2}$$
 (1.2)

where a is the graphene lattice constant, approximately 246 pm. The number of atoms N in the nanotube unit cell is also related to the chiral indices

$$N = \frac{4(n^2 + nm + m^2)}{\gcd(2n + m, 2m + n)}.$$
 (1.3)

Another key vector is the translational vector  $\mathbf{C}$ , perpendicular to  $\mathbf{A}$ , which defines the periodicity along the tube axis.

$$\mathbf{C} = n_c \mathbf{a_1} + m_c \mathbf{a_2} \,. \tag{1.4}$$

The relation between the chiral indices (n, m) and the indices  $(n_c, m_c)$  is determined by the condition that C is the shortest lattice vector perpendicular to

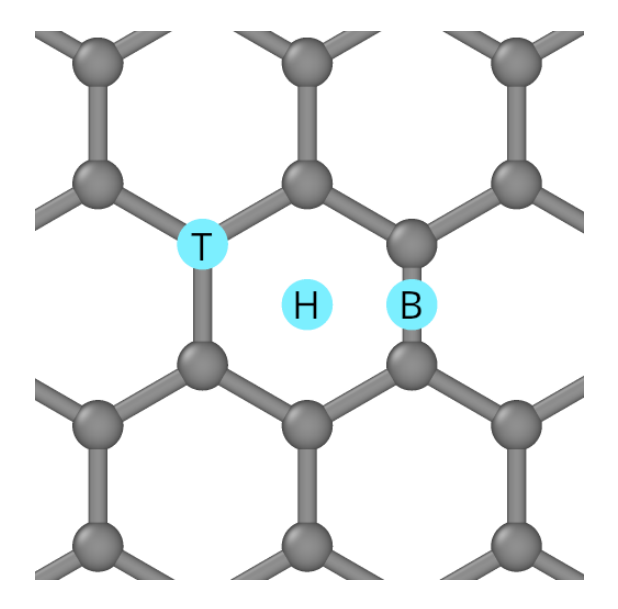


Figure 1.4: Graphene canonical adsorption sites: top (T), bridge (B), and hollow (H)

**A**. 
$$n_c = -\frac{2m+n}{\gcd(2m+n,2n+m)}, \quad m_c = \frac{2n+m}{\gcd(2m+n,2n+m)}. \tag{1.5}$$

Together, these vectors describe how the graphene sheet is rolled to form the nanotube, see Fig. 1.3, thereby determining its structural and electronic properties.

#### 1.2 Metal adsorption on graphene and nanotubes

On graphene, C-atoms hybridize in an  $sp^2$  configuration, forming  $\sigma$  bonds with three neighboring atoms. The orthogonal  $\pi$  orbitals form a delocalized electronic cloud above and below the surface, which can interact with adsorbed metal atoms and generate bonds with their d orbitals.

In literature it's possible to find *ab initio* studies of graphene adsorption with Cu and transition metals [18, 24] for their application as single atom catalysts. Cu-doped [5] can enhance reactivity and functionalized graphene becomes a very interesting structure for the synthesis of Quantum Dots [13]. Experimental studies on graphene interacting with transition metals [22, 19] shows agreement with DFT simulations.

The adsorption energy, lattice distortion, and Cu-C bond length depend on the relative position of the adatom. As Fig. 1.4 shows, we can distinguish different adsorption sites on graphene:

• Top (T): the adatom is located directly above a C-atom;

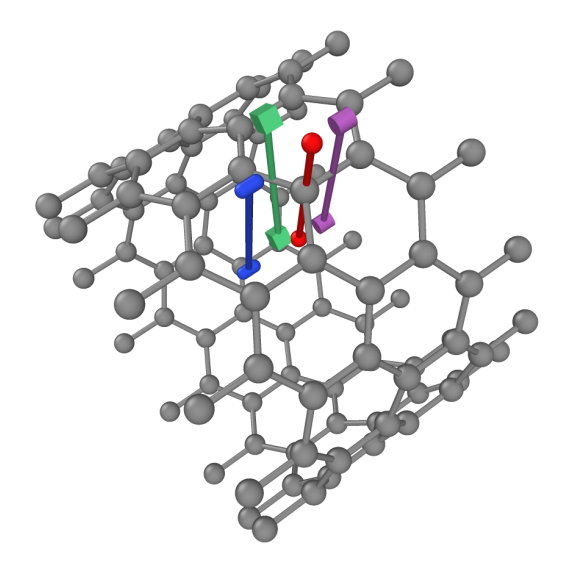


Figure 1.5: Internal and external adsorption sites of a zigzag CNT. Grey balls represent C-atom. Red spheres represent top sites, purple cylinders represent axial bridge sites, green cubes represent oblique bridge sites, and blue spheroids represent hollow sites. Non-grey sticks are for guiding the eyes and they are the relative projection on the tube surface.

- **Bridge** (B): The adatom is positioned above the midpoint of a C–C bond, hence the Cu binds with two C-atoms;
- Hollow (H): The adatom is placed above the center of a hexagonal carbon ring.

It's noteworthy that catalyst sites performance can be regulated by the carrier morphology [16]. On a curved surface such as a CNT, local curvature can enhance the interaction with an adsorbed atom. Adsorption energy tends to increase with curvature, meaning stronger binding. Indeed, the curvature of CNTs induces rehybridization of the orbitals, modifying the distribution of electrons [14] and sometimes generating a gap. For instance, on the convex side, the orbitals are more exposed to Cu d-orbitals, which may lead to stronger interactions. On the concave side, the  $\pi$  orbitals are oriented inward: although each individual orbital is less exposed, a larger number of orbitals may collectively point toward the adatom, potentially increasing the overall orbital overlap between CNT and adatom and strengthening the interaction.

On zigzag CNTs, we can distinguish T and H sites as above a graphene layer, while the curvature-induced symmetry breaking leads to two non-equivalent B sites, axial B1 and oblique B2, depending whether the C-C bond is parallel to

the tube axis or not, see Fig. 1.5. We further observe that the adsorption can occur external (ext-T, ext-B1, ...) or internal (int-T, int-B1, ...) the tube.

We found several DFT studies on the adsorption of Cu and other transition metal atoms [1, 26] as well as small clusters [4] on (8,0) CNTs. The reported adsorption energies for atoms on the external surface are approximately 0.5 eV, indicating a relatively weak interaction. Such energies are typical of physisorption: metal atoms are bound to the CNT surface without strong orbital hybridization, although some minor polarization effects may occur due to the proximity of the metal and the  $\pi$ -electron system of the CNT.

We select the zigzag (12,0) CNT for several practical and scientific reasons. First, its diameter is large enough to allow the adsorption of atoms inside the tube, enabling a direct comparison between internal and external binding sites. At the same time, it is not so large as to make the calculations computationally prohibitive, keeping the system tractable for DFT simulations. Moreover, the (12,0) tube still exhibits a noticeable curvature affecting the local electronic structure and the reactivity of the C-atoms. This therefore represents a good compromise between computational efficiency, chemical realism, and the ability to study curvature-dependent effects on adsorption.

## Chapter 2

## Methodology

In this chapter, we describe the theoretical framework and computational methods used to study the adsorption of copper atoms on carbon nanotubes. The primary tool employed is density functional theory (DFT), a quantum mechanical method widely used to investigate the electronic structure of many-body systems. Calculations are performed using the Quantum ESPRESSO package, which implements DFT with plane-wave basis sets and pseudopotentials. We discuss the choice of exchange-correlation functionals and numerical parameters to ensure accurate and reliable results.

#### 2.1 The DFT scheme

Our quantum-mechanical system is studied using DFT, which describes the electronic structure of many-body systems in terms of the electron density, rather than the full many-electron wavefunction. This approach drastically reduces computational complexity while maintaining high accuracy for ground-state properties. DFT is a well-established method in computational physics and chemistry and is widely used to investigate the electronic structure of atoms, molecules, and condensed matter systems.

#### 2.1.1 The Born-Oppenheimer approximation

The Born-Oppenheimer approximation can be applied to any Coulomb system to separate electronic and nuclear motions. It allows us to treat the nuclei as fixed while solving the electronic Schrödinger equation, threating the ionic field as external:

$$H = -\sum_{i} \frac{\hbar^{2}}{2m_{e}} \nabla_{i}^{2} + U + V_{\text{ext}} + E_{\text{nn}}, \qquad (2.1)$$

where U,  $V_{\text{ext}}$  represent the electron-electron and electron-nucleus interaction, respectively.  $E_{\text{nn}}$  depends only on the positions of the nuclei and is therefore independent of the electronic wavefunction.

The all-electrons Hamiltonian can be conceptually divided into simpler contributions:

$$H = T + V_{ext} + U \tag{2.2}$$

$$T = -\sum_{i} \frac{\hbar^2}{2m_e} \nabla_i^2 \quad V_{\text{ext}} = -\sum_{i,j} \frac{e^2 Z_j}{|\mathbf{r}_i - \mathbf{R}_j|} \quad U = \frac{1}{2} \sum_{i \neq j} \frac{e^2}{|\mathbf{r}_i - \mathbf{r}_j|}, \quad (2.3)$$

where T is the kinetic energy operator,  $V_{\text{ext}}$  represents the interaction with the external ionic field generated, each ion positioned in  $\mathbf{r}_j$  with atomic number  $Z_j$ , and U accounts for the electron-electron interaction. The system-specific information is contained in  $V_{\text{ext}}$ . The problem is many-body due to the presence of the electron-electron interaction U.

#### 2.1.2 The Hohenberg-Kohn theorems

The theoretical foundation of DFT is provided by the Hohenberg-Kohn (HK) theorems:

**HK1**: For a system of interacting electrons in a fixed external potential, the ground-state electron density  $n_0(\mathbf{r})$  uniquely determines the external potential  $V_{ext}(\mathbf{r})$  up to an additive constant.

**HK2**: The ground-state energy  $E_0$  is the unique minimum of the energy functional E[n], which is a functional of the electron density  $n(\mathbf{r})$ .

In other words, both the external potential  $V_{\text{ext}}$  and the ground-state wavefunction  $\psi_0$  are unique functionals of  $n(\mathbf{r})$ . Since knowledge of  $V_{ext}$  is sufficient to determine the ground state wavefunction, and the density is directly accessible, this implies a circular relation

$$n_0(\mathbf{r}) \leftrightarrow V_{\text{ext}}(\mathbf{r}) \leftrightarrow \psi_0$$
 (2.4)

in contrast to the usual unidirectional implication.

$$V_{\text{ext}}(\mathbf{r}) \to \psi_0 \to n_0(\mathbf{r})$$
. (2.5)

In general, the system information is contained in the more complex manybody density matrix  $\rho(\mathbf{r}_1,...,\mathbf{r}_N,\mathbf{r}_1',...,\mathbf{r}_N')$ , which can be reduced by tracing out all but a subset of electron coordinates, yielding a simpler object at the cost of losing some information. The diagonal of the one-body density matrix corresponds to the electron density

$$n(\mathbf{r}) = \rho(\mathbf{r}, \mathbf{r}) = N \int d\mathbf{r}_2 \dots d\mathbf{r}_N |\Psi(\mathbf{r}, \mathbf{r}_2, \dots, \mathbf{r}_N)|^2.$$
 (2.6)

The remarkable result of HK is that  $n(\mathbf{r})$ , when it is the ground-state density, encodes all the information about the system.

The total energy functional E[n] is defined as

$$E[n] = T[n] + U[n] + \int d\mathbf{r} V_{\text{ext}}(\mathbf{r}) n(\mathbf{r}), \qquad (2.7)$$

where T[n] and U[n] are the universal kinetic and interaction energy functionals, respectively. The ground-state energy  $E_0$  is obtained by minimizing E[n] with respect to  $n(\mathbf{r})$ , subject to the constraint that the total number of electrons is fixed:

$$\int n(\mathbf{r}) d\mathbf{r} = N. \tag{2.8}$$

The functional forms of T[n] and U[n] are not known explicitly, but approximations can be developed.

#### 2.1.3 The Kohn-Sham equations

Kohn and Sham (KS) proposed a practical approach to DFT by introducing a system of non-interacting electrons whose ground-state reproduces the same ground-state density as the interacting system. Such a system needs an effective interaction to account for the many-body phenomena. The KS equations can be derived from a minimization problem.

The energy of the system to minimize is a functional of the electron density

$$E_{KS} = T[n] + U[n] + \int d\mathbf{r} V_{\text{ext}}(\mathbf{r}) n(\mathbf{r})$$
 (2.9)

$$T[n] + U[n] = T_s[n] + E_H[n] + E_{xc}[n],$$

where  $T_s[n]$  is the non-interacting system kinetic energy,  $E_H[n]$  is the Harthree energy

$$E_H = \frac{e^2}{2} \int \frac{d\mathbf{r} \, n(\mathbf{r}) \, d\mathbf{r}' \, n(\mathbf{r}')}{|\mathbf{r} - \mathbf{r}'|}, \qquad (2.10)$$

and the  $E_{xc}[n]$  term is the exchange-correlation energy functionals that includes all the ignored terms of the functional that account for the Coulomb exchange, kinetic variation  $T - T_s$ , and the electronic correlation.

Since the particles are non-interacting, the ground state will be the Slater determinant of orbitals  $\{\phi_i\}$  that minimize the functional  $E_{KS}[n]$ , with the orthonormality constraint

$$\langle \phi_i | \phi_j \rangle = \delta_{ij} \,. \tag{2.11}$$

It's possible to write the Lagrangian, a functional of the KS orbitals that merges the  $E_{KS}$  with a Lagrange multiplier term

$$\mathcal{L}[\{\phi_i\}, \{\varepsilon_{ij}\}] = E_{KS} - \sum_{i,j} \varepsilon_{ij} (\langle \phi_i | \phi_j \rangle - \delta_{ij}). \qquad (2.12)$$

The derivation of the KS equations follows requiring the stationarity of this functional

$$\frac{\delta \mathcal{L}}{\delta \phi_i^*(\mathbf{r})} = 0 \quad \forall i \,. \tag{2.13}$$

These are the partial derivatives of each functional relative to  $\phi_i^*$  orbital:

$$\frac{\delta T_s}{\delta \phi_i^*(\mathbf{r})} = -\frac{\hbar^2}{2m_e} \nabla^2 \phi_i(\mathbf{r}) \qquad \text{kinetic term,}$$
 (2.14)

$$\frac{\delta}{\delta \phi_i^*(\mathbf{r})} \int d\mathbf{r}' V_{\text{ext}}(\mathbf{r}') n(\mathbf{r}') = V_{\text{ext}}(\mathbf{r}) \phi_i(\mathbf{r}) \quad \text{external field term}, \tag{2.15}$$

$$\frac{\delta E_H}{\delta \phi_i^*(\mathbf{r})} = V_H(\mathbf{r})\phi_i(\mathbf{r}) = e^2 \int \frac{d\mathbf{r}' n(\mathbf{r}')}{|\mathbf{r} - \mathbf{r}'|} \phi_i(\mathbf{r}) \quad \text{Hartree potential term}, \tag{2.16}$$

$$\frac{\delta E_{\rm xc}}{\delta \phi_i^*(\mathbf{r})} = V_{\rm xc}(\mathbf{r})\phi_i(\mathbf{r}) \qquad \text{exchange-correlation term.} \quad (2.17)$$

Summing all contributions in Eq. 2.13 leads to the effective single-particle Kohn–Sham equation:

$$H\phi_i(\mathbf{r}) = \left(-\frac{\hbar^2}{2m_e}\nabla^2 + V_{\text{ext}}(\mathbf{r}) + V_H(\mathbf{r}) + V_{\text{xc}}(\mathbf{r})\right)\phi_i(\mathbf{r}) = \varepsilon_i\phi_i(\mathbf{r}), \qquad (2.18)$$

which represents an eigenvalue problem for the auxiliary Hamiltonian H. Its eigenfunctions  $\phi_i(\mathbf{r})$  are the Kohn–Sham orbitals, and the eigenvalues  $\varepsilon_i$  correspond to the energies of the non-interacting reference system. These eigenvalues themselves are not directly physically meaningful, as they originate from the Lagrange multipliers enforcing orbital orthonormality. The Kohn–Sham orbitals are instead used to reconstruct the electron density

$$n(\mathbf{r}) = \sum_{i} |\phi_i(\mathbf{r})|^2, \tag{2.19}$$

Pseudopotentials are commonly employed to simplify the treatment of core electrons, focusing on valence electrons, which primarily determine chemical bonding and material properties. The pseudopotentials replace the all-electron potential with a smoother effective potential, reducing the number of electrons and

simplifying the computational effort. This leads to significant modifications in the KS equations, but the overall framework remains unchanged.

#### 2.1.4 Solution to the Kohn-Sham equations

The KS equations are solved self-consistently through an iterative procedure:

- 1. Start with an initial guess for the electron density  $n(\mathbf{r})$ .
- 2. Construct the effective Hamiltonian H using the current density.
- 3. Solve the KS equations to obtain new orbitals  $\phi_i(\mathbf{r})$  and eigenvalues  $\epsilon_i$ .
- 4. Update the electron density using the new orbitals and their occupation numbers.
- 5. Check for convergence: if the density (or energy) has not changed significantly, stop; otherwise, return to step 2.

After some iterations, the obtained  $n(\mathbf{r})$  is a (scalar) self consistent field (SCF).

Expanding the KS orbitals in a suitable basis set, such as plane waves or localized atomic orbitals, transforms the differential equations Eq. 2.18 into a matrix diagonalization problem that can be solved numerically. In the present thesis we will adopt the plane-waves basis, as implemented in the Quantum Espresso [7, 6, 8] method.

#### The plane waves method

The plane-wave method [17] is commonly adopted to take advantage of periodicity. The total effective potential,

$$V_{KS}(\mathbf{r}) = V_{ext}(\mathbf{r}) + V_H[n](\mathbf{r}) + V_{xc}[n](\mathbf{r}), \qquad (2.20)$$

must be periodic. Luckily, if the external potential  $V_{\text{ext}}(\mathbf{r})$  is periodic and the electron density  $n(\mathbf{r})$  inherits the same periodicity, then both the Hartree potential  $V_H[n](\mathbf{r})$  and the exchange-correlation potential  $V_{\text{xc}}[n](\mathbf{r})$  will automatically be periodic as well. Consequently, the total Kohn–Sham potential  $V_{\text{KS}}(\mathbf{r})$  is periodic, allowing the efficient use of plane-wave basis sets.

According to Bloch's theorem, it is possible to express each orbital in terms of a periodic  $u_{jk}$  modulating a plane-wave factor

$$\phi_{n\mathbf{k}}(\mathbf{r}) = e^{i\mathbf{k}\cdot\mathbf{r}} u_{n\mathbf{k}}(\mathbf{r}). \tag{2.21}$$

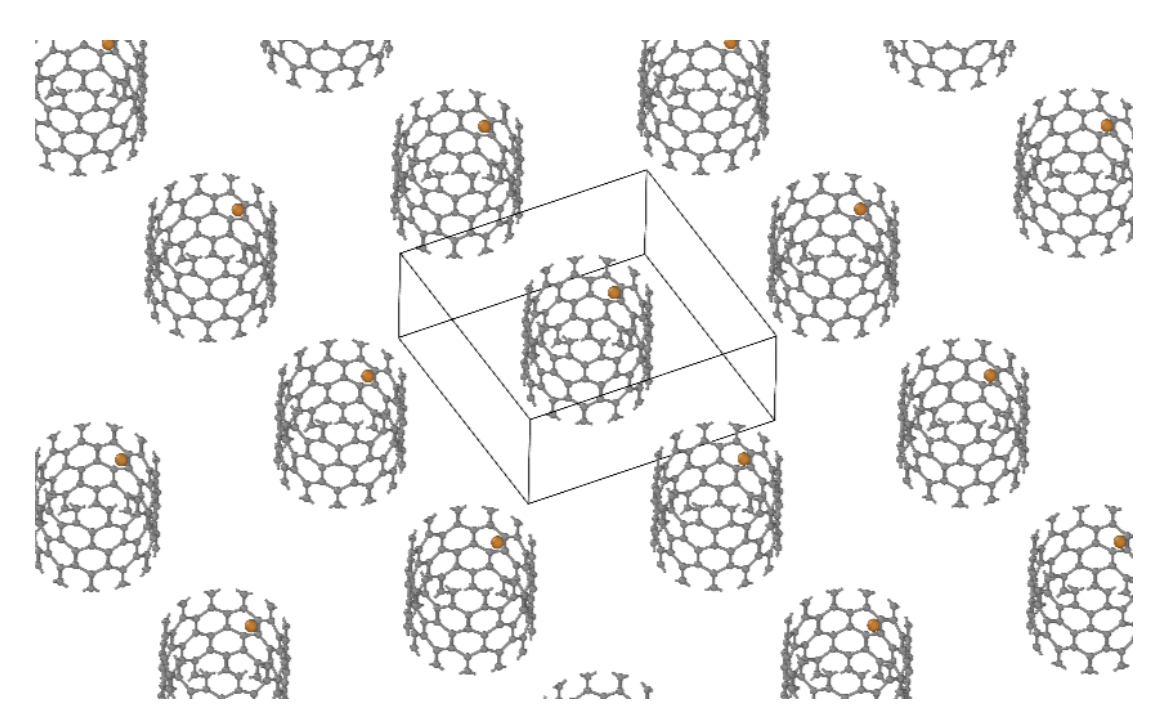


Figure 2.1: Periodic boundary conditions of the Cu/CNT. Box highlighted in grey lines. C-atoms and Cu-adatom are in grey and orange balls, respectively. Only the xy repetitions are depicted.

A detailed analysis of the KS equation shows that it can be reformulated in the following equation for the periodic terms:

$$H^{(\mathbf{k})}u_{n\mathbf{k}}(\mathbf{r}) = \left[ -\frac{\hbar^2}{2m_e} (\nabla + i\mathbf{k})^2 + V_{KS}(\mathbf{r}) \right] u_{n\mathbf{k}}(\mathbf{r}) = \varepsilon_{n\mathbf{k}} u_{n\mathbf{k}}(\mathbf{r}).$$
 (2.22)

The wavevector  $\mathbf{k}$  is restricted to the first Brillouin zone (1BZ) of the reciprocal lattice. This allows one to solve periodic problems in a single unit cell with periodic boundary conditions on  $u_{n\mathbf{k}}$ .

The matrix elements of the Kohn-Sham Hamiltonian in the plane-wave basis are

$$H_{\mathbf{k}\,\mathbf{k}'} = \langle \mathbf{k}|H[n]|\mathbf{k}'\rangle = \langle \mathbf{k}|T_{s}|\mathbf{k}'\rangle + \langle \mathbf{k}|V_{KS}[n]|\mathbf{k}'\rangle =$$

$$= \delta_{\mathbf{k}\,\mathbf{k}'} \frac{\hbar^{2}\mathbf{k}^{2}}{2m_{e}} + \int e^{-i\mathbf{k}\cdot\mathbf{r}}V_{KS}[n]e^{i\mathbf{k}'\cdot\mathbf{r}} d\mathbf{r} = \delta_{\mathbf{k}\,\mathbf{k}'} \frac{\hbar^{2}\mathbf{k}^{2}}{2m_{e}} + \tilde{V}_{\text{eff}}(\mathbf{k} - \mathbf{k}'),$$
(2.23)

where  $\tilde{V}_{KS}$  is the Fourier transform of  $V_{KS}$ . Since under periodic boundary conditions  $V_{\text{eff}}$  is cell-periodic, see Fig. 2.1, its Fourier transform  $\tilde{V}_{KS}$  is actually a discrete Fourier series: the potential matrix elements vanishes unless  $\mathbf{k} - \mathbf{k'}$  is a reciprocal lattice vector  $\mathbf{G}$ . This allows us to divide the continuum matrix into blocks, each corresponding to one  $\mathbf{k} \in 1BZ$ , with non-trivial off-diagonal elements.

This approach naturally follows the scheme suggested by the Bloch theorem to divide the problem into many matrices, one for each  $\mathbf{k}$  in the 1BZ:

$$\left\{ H_{\mathbf{G},\mathbf{G}'}^{(\mathbf{k})} \right\} = \begin{pmatrix} \ddots & \vdots & \vdots & \ddots \\ \cdots & T_{s}(\mathbf{k} + \mathbf{G}_{i}) + \tilde{V}_{\text{eff}}(\mathbf{0}) & \tilde{V}_{\text{eff}}(\mathbf{G}_{i} - \mathbf{G}_{i+1}) & \cdots \\ \vdots & \vdots & \ddots & \vdots \\ \vdots & \vdots & \ddots & \vdots \end{pmatrix}, (2.24)$$

where **G** are the reciprocal lattice vectors of the periodically repeated simulation cell,  $T_s(\mathbf{k} + \mathbf{G}) = \frac{\hbar^2}{2m_e} |\mathbf{k} + \mathbf{G}|^2$  is the kinetic energy term.

For the Cu/CNT system the periodicity along the x and y axis is artificially introduced by the plane wave basis, so no 1BZ sampling is needed along  $k_x$  and  $k_y$  reciprocal axis. The only physical periodicity is along the z axis: we sample the k-points only along  $k_z$ .

#### 2.1.5 Precision and accuracy of DFT

Obtaining reliable results from DFT calculations requires a careful choice of functionals, pseudopotentials, and numerical parameters.

The one-body KS equations are an approximation to the many-body problem, and the exact form of the exchange-correlation functional is unknown. This constitutes an intrinsic limitation to the accuracy of DFT.

Additionally, computational resources limit the achievable precision and accuracy of the calculations. Pseudopotentials introduce further approximations by replacing the complex all-electron potential with a smoother effective potential acting on valence electrons. Simulation parameters, such as energy cutoffs and  $\mathbf{k}$ -point sampling, also affect the precision of the results.

#### **Functionals**

Developing approximate functionals remains an active research field, with many different approaches. There are several families of functionals, each with its own strengths and weaknesses. Some exact conditions exist that functionals should satisfy to ensure physical consistency, but no functional is perfect.

A simple early approximation to the exchange-correlation functional was the Local Density Approximation (LDA), which assumes that the exchangecorrelation energy at each point in space depends only on the local electron density.

For the Homogeneous Electron Gas model (HEG), the exchange-correlation energy per particle depends only on the density n of the system. What the LDA does is to use the HEG model locally, assuming that the density varies slowly in space:

$$\epsilon_{\rm xc}^{LDA}[n](r) = \epsilon_{\rm xc}^{HEG}(n(\mathbf{r}))$$
 (2.25)

Since LDA can sometimes yield relatively poor results for inhomogeneous systems, the Generalized Gradient Approximation (GGA) was developed, which includes the gradient of the electron density to account for spatial variations:

$$\epsilon_{\rm xc}^{GGA}\left(n({\bf r}), \nabla n({\bf r})\right)$$
 (2.26)

Probably the most widely used GGA functional is the Perdew-Burke-Ernzerhof (PBE) functional, which was constructed to satisfy several known exact conditions for the exchange-correlation energy. Since the community has extensively tested it and it provides a good balance between accuracy and computational cost, we adopt the PBE functional in this work.

#### 2.1.6 Numerical parameters

Adopting appropriate numerical parameters is crucial to ensure the precision and accuracy of DFT calculations. Each calculation involves different stages, so several parameters must be considered. A few important parameters for the numerical solution of the KS equation:

- Plane-waves basis-set cutoff: in Eq. (2.24) the Hamiltonian matrix  $H^{(k)}$  is discrete but still infinite. A cutoff energy  $E_{\text{cut}}$  is introduced to limit the number of plane waves in the basis set, since the incidence of high-energy plane waves is negligible for the expansion of the KS orbitals. A larger base gives a more precise matrix, but is also more computationally expensive to diagonalize.
- Density energy cutoff: the charge density is also represented using a plane-wave basis set that typically requires a higher energy cutoff than the wavefunctions. For PAW pseudopotentials, it is common to set the density cutoff to 8 times the wavefunction cutoff. A higher cutoff ensures a more accurate Hamiltonian construction at each step of the SCF cycle.
- **k-points sampling**: the set  $\{H^{(k)}\}_{k\in 1BZ}$  has infinite elements, so the **k**-points are sampled on a finite grid called *mesh*. The computational cost

increases linearly with the number of  $\mathbf{k}$ -points, but parallelization is near-optimal: linear scaling of the time complexity with little overhead. System symmetries can also be exploited to reduce the number of  $\mathbf{k}$ -points required.

• SCF convergence thresholds: The cycle should employ strict convergence criteria to ensure that the electronic structure is accurately determined. Typical thresholds range from 10<sup>-6</sup> to 10<sup>-10</sup> Ry for the total energy change between successive iterations to terminate the self-consistency loop.

After each SCF calculation, results can be used to perform geometrical optimization, reorganizing ions positions and cell parameters to search for minimum-energy configuration. A few important parameters for structural optimization:

- Ionic relaxation parameters: the structure undergoes relaxation to determine suitable equilibrium positions of the ions in the cell. Various algorithms can be adopted to find an optimal geometry: for this work the Broyden-Fletcher-Goldfarb-Shanno (BFGS) [21] algorithm is adopted.
- Cell relaxations parameters: the PBC introduce stresses acting on the structure, resulting in unwanted pressure on the supercell namely the trace of the stress tensor. The same BFGS algorythm is adopted to relax the cell parameters and reach a target pressure, generally  $\sim 0$ . For the present 1-dimensional problem, the lateral (xx) and yy stress components are irrelevant (as long as the replicas do not interact they should be very small anyway), and only the zz stress component along the CNT axis must be relaxed to 0.
- Relaxation thresholds: to determine convergence of the structural relaxation, the energy difference between successive steps must fall below a threshold, and the total forces on the atoms as well as the pressure acting on the cell must be sufficiently small. In typical plane-wave DFT calculations, these criteria correspond to energy changes of  $10^{-3}$   $10^{-4}$  Ry, maximum forces below  $10^{-3}$  Ry/ $a_0$ , and pressures  $\leq 0.5$  kbar, ensuring that the system is not too far from a stable geometry.

#### 2.2 The QuantumESPRESSO package

The QuantumESPRESSO (QE) package is a widely used, integrated suite of open-source software for electronic structure calculations. It centers around pw.x, a computer program that implements the plane waves method to solve the KS pseudopotential equations within the DFT framework.

Its strength lies in the fact that calculations are performed in reciprocal space, which simplifies the solution of the equations. The plane-wave basis set is particularly suitable for periodic systems, as band structure calculations are straightforward.

Periodicity also allows for near-optimal parallelization. The KS equations are transformed into a Bloch problem and solved for each 1BZ divided in *pools*, sets of **k**-points on a single QE parallel process. The best scaling factor is obtained putting one singular **k**-point i each *pool*. While perfectly suited for crystalline systems, the main disadvantage of plane waves is that they imply PBCs even for finite systems. This can lead to artifacts or excessive memory and computation time usage.

The QE package is highly flexible, enabling calculations on a wide variety of systems, including crystals, surfaces, and molecules. Given the pseudopotentials and atomic positions, QE evaluates the ground-state electronic structure, total electron energy, andion-ion interactions neglected by the Born-Oppenheimer approximations. It calculates orces on the ions and many other relevant properties, and also supports geometry optimization and a range of additional tasks.

#### 2.2.1 The pw.x input file

pw.x reads an input file that specifies the atomic positions, the modeling parameters, and selects the desired kind of calculation. In the following some snippets from QE input files, with comments on the right side of the pages. Those are from a relax (Relaxation) simulation, except for the CELL section which is peculiar of vc-relax (Variable Cell Relaxation) simulations.

```
&CONTROL
    calculation = 'relax'
    prefix = 'CNT_12_0_2_Cu_random_relaxed'
    outdir = './OUTPUTS/'
    pseudo_dir = './pseudos'
    tprnfor = .true.
    tstress = .true.
    etot_conv_thr = 1e-4
    forc_conv_thr = 1e-4
//
```

Control section: general instructions about the kind of calculation, file names, directories, and convergence thresholds.

```
&SYSTEM
    ibrav = 6
    A = 21.0
    C = 8.541458542294
    nat = 97
    ntyp = 2
    ecutwfc = 60.0
    ecutrho = 480.0
    occupations = 'smearing'
    smearing = 'mp'
    degauss = 0.0001
&ELECTRONS
    conv_thr = 1.0e-10
    mixing_beta = 0.5
    startingwfc = 'atomic+random'
&IONS
    ion_dynamics = 'bfgs'
    cell_dynamics = 'bfgs'
    press = 0.2
    cell_dofree = 'z'
ATOMIC_SPECIES
    C 12.011 C.pbe-n-kjpaw_psl.1.0.0.UPF
    Cu 63.546 Cu.pbe-kjpaw.UPF
ATOMIC_POSITIONS {angstrom}
C 1.5240257290e+01 1.0500000000e+01 1.200...
C 1.4604962079e+01 1.2870002938e+01 1.422...
C 1.5078702546e+01 1.1726866125e+01 2.136...
Cu 1.34051250e+01 1.615751250e+01 3.05782...
K_POINTS automatic
```

System section: lattice kind and parameters, number and types of atoms, energy cutoffs, and smearing settings.

Electronic parameters: SCF convergence threshold, mixing factor, and initial guess for the wavefunctions.

**Ions section**: parameters for ionic relaxation or molecular dynamics simulations.

Cell section: parameters for cell optimization, used in variable-cell relaxations.

Atomic species section: specifies the types of atoms, their masses, and the names of the files containing the pseudopotentials used.

Atomic positions section: lists the coordinates of each atom in the unit cell.

**k-points section**: specifies the **k**-point mesh of the 1BZ, that sets the fineness of the sampling of the electronic bands.

#### 2.2.2 The pw.x output file

1 1 25 0 0 0

The output file generated by pw.x contains detailed information about the calculation, including SCF steps, geometry optimization steps, the final total energy, forces on atoms, the stress tensor, and other relevant properties. The following snippets are from a relax simulation.

Initial potential from superposition of free atoms

starting charge 394.9957, renormalised to 395

negative rho (up, down): 2.650E-03 0.000E+00 Starting wfcs are 393 randomized atomic wfcs Checking if some PAW data can be deallocated...

total cpu time spent up to now is 187.4 secs

Self-consistent Calculation

iteration # 1 ecut= 60.00 Ry beta= 0.50
Davidson diagonalization with overlap
ethr = 1.00E-02, avg # of iterations = 2.0

negative rho (up, down): 2.704E-03 0.000E+00

total cpu time spent up to now is 548.4 secs

total energy = -1924.52084521 Ry estimated scf accuracy < 72.77415601 Ry

iteration # 2 ecut= 60.00 Ry beta= 0.50

. .

iteration # 32 ecut= 60.00 Ry beta= 0.50
Davidson diagonalization with overlap
ethr = 1.53E-13, avg # of iterations = 4.9

negative rho (up, down): 3.996E-03 0.000E+00

total cpu time spent up to now is 10367.5 secs

 ${\tt End\ of\ self-consistent\ calculation}$ 

After listing the input parameters, the output file shows the progress of the SCF calculation, the total energy at each iteration, the convergence status, and the final energy for that configuration.

The first SCF convergence is usually more difficult to achieve because it starts from a random guess for the wavefunctions.

```
Once the SCF cycle is fin-
     k = 0.0000 \ 0.0000 \ 0.0000 \ (199335 \ PWs) bands (eV):
-21.5845 -21.1122 -21.0888 -20.7791 -20.7316 -20.214...
                                                                    ished, meaning that the
-20.0063 -19.6510 -19.6445 -19.6214 -19.6160 -19.333...
                                                                    energy change between two
                                                                    consecutive iterations is
                                                                    below the specified thresh-
-0.2581 0.0905 0.0999 0.7219 0.7400 0.7910...

    1.2751
    1.4573
    1.8137
    1.9627
    2.0048
    2.0214...

    2.1373
    2.2111
    2.3711
    2.5073
    2.5973
    2.6388...

    2.9510
    2.9845
    3.0880
    3.1203
    3.1427
    3.1958

                                                                    old (10^{-10} \,\mathrm{Ry}), the out-
                                                                    put file displays the final
                                                                    results of the calculation:
     k = 0.0000 \ 0.0000 \ 0.0983 \ (199423 \ PWs) bands (eV):
                                                                    electronic bands, Fermi en-
-21.5824 -21.1099 -21.0865 -20.7771 -20.7293 -20.23...
                                                                    ergy, forces on atoms, and
-19.9134 -19.7610 -19.7320 -19.5301 -19.5014 -19.42...
 -19.2420 -19.1738 -19.1529 -18.7995 -18.7758 -18.57...
                                                                    the stress tensor.
  the Fermi energy is -1.3407 eV
                      = -1982.92319363 Ry
  total energy
  total all-electron energy = -10625.033544 Ry
 total all-electron charges constant that all-electron charges consistent with the second constant (-TS) = 0.00000135 Ry
  internal energy E=F+TS = -1982.92319498 Ry
  The total energy is F=E-TS. E is the sum of the following contributions:
  one-electron contribution = -10573.36847749 Ry
  hartree contribution = 5357.16692043 Ry
                            = -464.48534875 Ry
  xc contribution
  ewald contribution = 4386.00695348 Ry
  one-center paw contrib. = -688.24324266 Ry
  convergence has been achieved in 32 iterations
```

negative rho (up, down): 3.996E-03 0.000E+00

```
Forces acting on atoms (Cartesian axes, Ry/au):
           1 type 1 force =
                                         0.00...
                             -0.00025336
    atom
                            0.00315002 -0.00...
           2 type 1 force =
    atom
                   0.117312
    Total force =
                            Total SCF correction...
    Computing stress (Cartesian axes) and pressure
    negative rho (up, down): 3.996E-03 0.000E+00
        total stress (Ry/bohr**3) ...
  0.00000748 -0.00000148 -0.00000044 ...
 (kbar) P=
             -0.22
       1.10
                           -0.07
                 0.66 -0.14
       -0.22
 . . .
       -0.07 -0.14
                           2.97
    BFGS Geometry Optimization
                              0.0E+00 Ry
    Energy error
                             6.2E-02 Ry/Bohr
    Gradient error
    Number of SCF cycles = 1
    Number of BFGS steps
                    new = -1982.9231936334 Ry
    Energy
    New trust radius
                               0.0720412010 bohr
    New conv_thr
                                   1.0E-10 Ry
ATOMIC_POSITIONS (angstrom)
         15.2401232151
                           10.5006327460
                                             0...
С
          14.6066290001
                          12.8689609508
                                              1...
```

. . .

Relaxation calculations (relax, vc-relax) show the updated atomic positions after each step, obtained using the BFGS algorithm. Note that this is not a molecular dynamics simulation: the movements do not represent physical trajectories, they are purely numerical steps to locate the minimum-energy configuration.

Here follows one last frame from a vc-relax simulation.

```
2.7E-04 hy
1.7E-03 Ry/Bohr
Energy error
Gradient error
Cell gradient error =
                           4.1E-01 kbar
Number of SCF cycles = 4
Number of BFGS steps = 3
Enthalpy
               old = -884.9679280048 Ry
Enthalpy
               new = -884.9681994660 Ry
CASE: enthalpy _new < enthalpy
                                            _old
New trust radius
                           0.0077912509 bohr
New conv_thr
                                 2.7E-12 Ry
New unit-cell volume = 12721.53201 a.u.^3 ( 1885.1365...
Density = 0.50784 g/cm<sup>3</sup>
CELL_PARAMETERS (alat= 39.68424862)
  1.000000000 0.000000000 0.000000000
  0.00000000 1.00000000 0.00000000
   0.00000000 0.00000000 0.203556479
```

When performing a variable-cell relaxation (vc-relax), a few differences appear in the output file, as the cell parameters are also optimized.

At this stage, the output file may continue with additional ionic steps until convergence is reached, or it may terminate if the maximum number of ionic steps is reached without achieving convergence. The calculation can be restarted from the last configuration using the restart option in the &CONTROL section of the input file.

Upon completion, several files are generated in the specified output directory, containing information on KS states, charge density, potentials, and other relevant data for restarting, further analysis, or post-processing.

## Chapter 3

## Setup

We carry out input file preparation and low-memory data analysis on our personal computer. We perform heavy calculations, including simulations and post-processing, running QE on a parallel-computing cluster, provided by *Indaco*, a high-performance computing facility at *Università degli Studi di Milano*.

#### 3.1 The atomic configuration

We generate the initial atomic configuration of the (12,0) CNT for QE simulations with a custom C++ program, see Appendix A, that outputs atomic coordinates in standard XYZ format, see Fig. 3.1 for a few examples. This program takes as input the chiral indices (n,m), the number of unit cell repetitions, and the lattice parameter. This program constructs the CNT by rolling a graphene sheet according to the selected chirality, placing C-atoms at the appropriate positions in three-dimensional space. It also provides the correct length of the z box-side to use in calculations in order to properly maintain the PBC.

Since the structural parameters (e.g. the C-C spacing) assumed by the CNT generator are not precisely the optimal ones, the CNT structure needs to undergo a full vc-relax to clear the internal strains and reach its optimal equilibrium geometry. The length of the periodically repeated CNT unit amounts to L=854 pm. The CNT diameter is 948 pm. As a successive step, we insert the Cu adatom, and execute a full relaxation of its position, as well as of those of all CNT atoms.

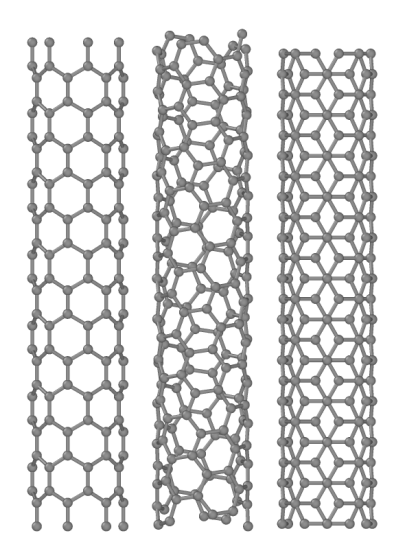


Figure 3.1: CNT generated with our custom C++ code, from left to right a zigzag, chiral, and armchair.

#### 3.2 Setting up the calculations

To have meaningful adsorption data we need to define the parameters to be used in QE. Here we report the so-called *convergence tests* needed for setting the correct input parameters.

#### 3.2.1 Convergence tests

As discussed in Sec. 2.1.6, several numerical approximations affect the accuracy of DFT simulations. To ensure that the uncertainty on the total energy remains below 0.01 eV, we perform systematic convergence tests on basis energy cutoffs, tube-tube distance, smearing and **k**-points mesh density.

The scheme we adopt is to perform numerous SCF calculations on a specific structure, varying one parameter at a time, while keeping the others fixed. The total energy for each tested value is compared with the one of a reference system, with that parameter set to obtain a highly precise, very expensive, calculation.

#### 3.2.2 Energy cutoff

The basis-set convergence is a critical task for any quantum-mechanical simulation. For plane-wave DFT calculations, this translates in one parameter, the energy cutoff ecutwfc, which controls the plane-wave basis set. We perform a set of calculations on a C-Cu dimer with increasing cutoff values: the resulting

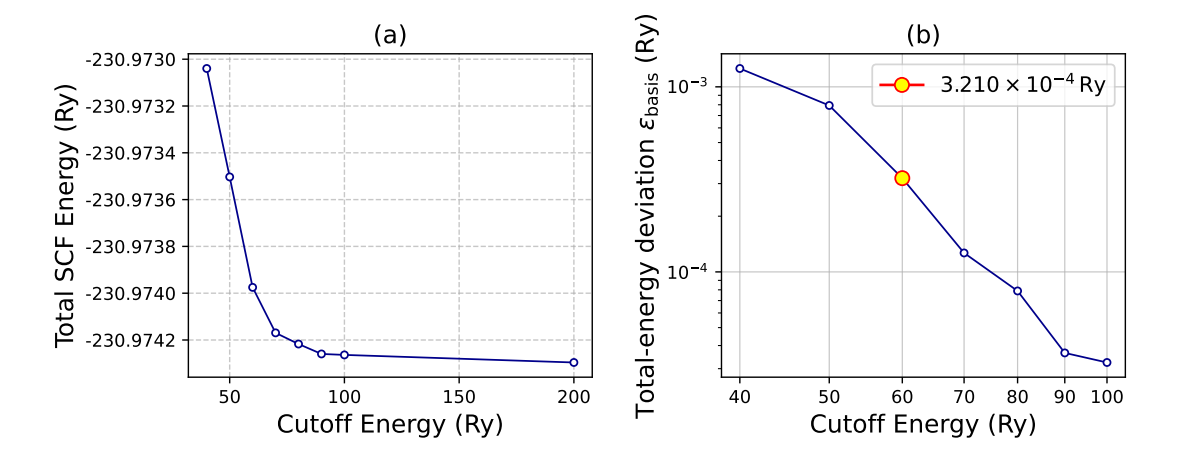


Figure 3.2: (a): the total SCF energy estimation of a C–Cu dimer as a function of the wavefunction energy cutoff. (b): the SCF energy precision at each cutoff, obtained by taking the 200 Ry-cutoff simulation as a reference. The final adopted cutoff is highlighted.

total energy is reported in Fig. 3.2(a).

For PAW pseudopotentials, the density cutoff ecutrho is usually set to eight times the wavefunction cutoff. A finer sampling modestly increases the computational cost but prevents aliasing effects and guarantees a well-defined Hamiltonian.

Because the single Cu atom, with its localized d-electrons, dominates the basis-set requirements, the error estimated on the C–Cu dimer can be directly transferred to the Cu/CNT system, neglecting errors coming from C-atoms.

Eventually, we adopt a 60 Ry cutoff, which results in a deviation on the total energy of

$$\varepsilon_{\text{basis}} = 3.21 \times 10^{-4} \text{ Ry} \simeq 4.5 \text{ meV},$$
 (3.1)

as illustrated in Fig. 3.2(b).

#### 3.2.3 Cell size

Periodic boundary conditions along z reproduce the nanotube's intrinsic periodicity. In the xy plane, however, replicas of the tube interact unless sufficient vacuum is added, leading to artificial lateral stresses.

We adopt a 2.1 nm side length of the simulation box that gives a negligible  $8\times 10^{-6}~{\rm Ry}~(\sim 0.1~{\rm meV})$  error, by comparing with a larger 4 nm cell. The lateral nanotube-nanotube interactions, see Fig. 2.1, can affect dramatically the adsorption properties of adatoms, especially when placed outside the CNT. To

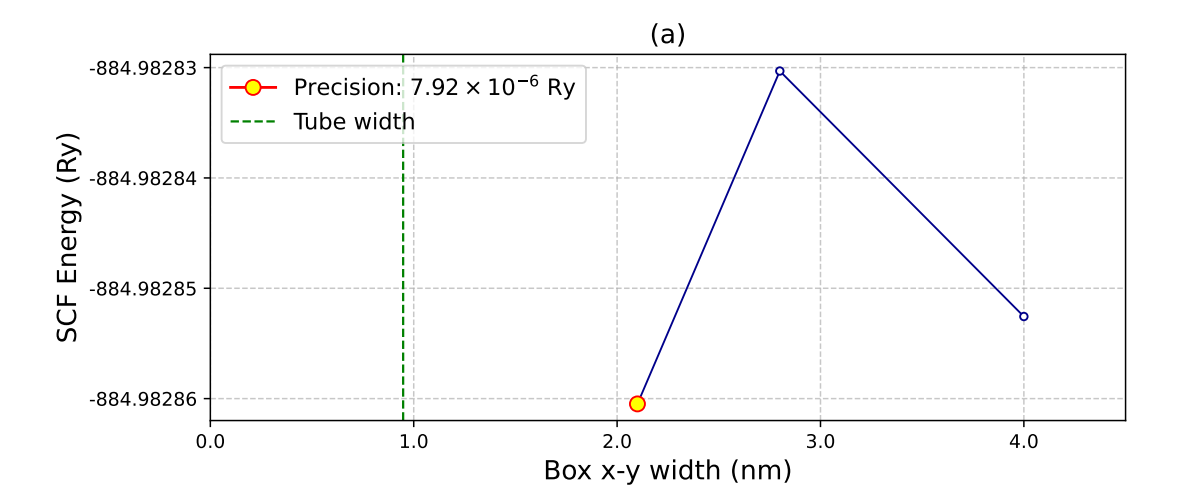


Figure 3.3: Total scf energy estimation of a pure (12, 0) relaxed CNT unit cell as a function of the lateral (x) and y, orthogonal to the CNT axis) box size. The CNT width is represented by a green vertical line. Highlighted point: the selected size. The relative error estimation is obtained by taking the 4 nm simulation as a reference.

$$\begin{pmatrix} -0.45 & 0.00 & 0.00 \\ & -0.45 & 0.00 \\ & & 0.24 \end{pmatrix} \qquad P = -0.22$$

Table 3.1: Residual stress tensor and total pressure acting on the relaxed CNT, expressed in kbar.

prevent these spurious effect, we prefer to keep the CNT replicas well spaced, even at the cost of a more expensive basis set. The relaxed structure exhibits only negligible interactions with its periodic images, see Tab. 3.1, indicating that the chosen cell size is sufficient to prevent artificial effects on the adsorption properties. The cell size in the z direction is determined later by zeroing the axial stress of a pure (no adsorbate) CNT, as discussed below.

#### 3.2.4 k-point sampling

Accurate 1BZ sampling along the tube axis is essential. We recalculate the total energy of the pristine relaxed nanotube for various different **k**-points meshes along  $k_z$  axis. The purpose of these simulations is to ensure bulk-like behavior in

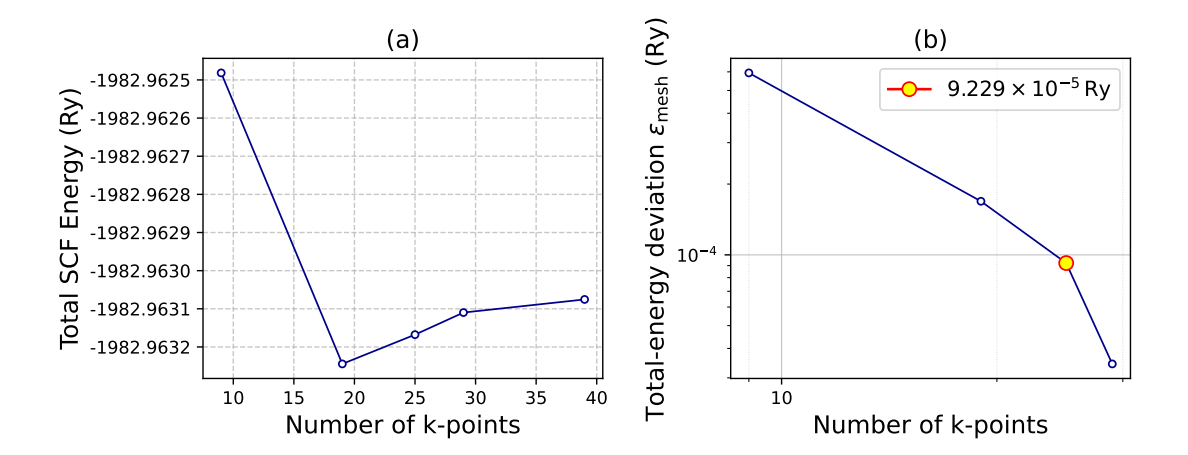


Figure 3.4: (a): the total SCF energy estimation of the pristine 0.84 nm (12, 0) CNT as a function of the number of  $\bf k$  points in the adopted mesh. (b): the SCF energy precision for each mesh, obtained by taking the 90  $\bf k$  points-simulation as a reference. The final adopted mesh is highlighted.

the direction z of CNT periodicity. The mesh we adopt will guarantee reliable electronic-structure results while keeping the computational effort under control. Eventually, we adopt a 25 **k**-points mesh, see Fig. 3.4 responsible for an estimated error contribution of

$$\varepsilon_{\rm mesh} = 9.23 \times 10^{-5} \text{ Ry} \simeq 1.3 \text{ meV}.$$
 (3.2)

In practice, thanks to symmetry, the mesh consists of only 13 irreducible k-points.

#### 3.2.5 Smearing

To improve electronic convergence in metallic or small-gap systems, a smearing technique is employed. Smearing distributes occupation numbers around the Fermi level, avoiding discontinuities in the electronic density that can hinder self-consistent convergence. The width of this distribution, defined by the parameter degauss, controls the energy broadening, directly affecting SCF stability. We adopt a 0.0001 Ry smearing, resulting in an estimater error of

$$\varepsilon_{\text{smearing}} = 9.20 \times 10^{-5} \text{ Ry} \simeq 1.3 \text{ meV}.$$
 (3.3)

.

We estimate the total error on the total energy as a composition of basis, mesh and smearing contribution:

$$\varepsilon_{\text{tot}} = \varepsilon_{\text{basis}} + \varepsilon_{\text{mesh}} + \varepsilon_{\text{smearing}} \sim 7 \text{ meV}.$$
 (3.4)

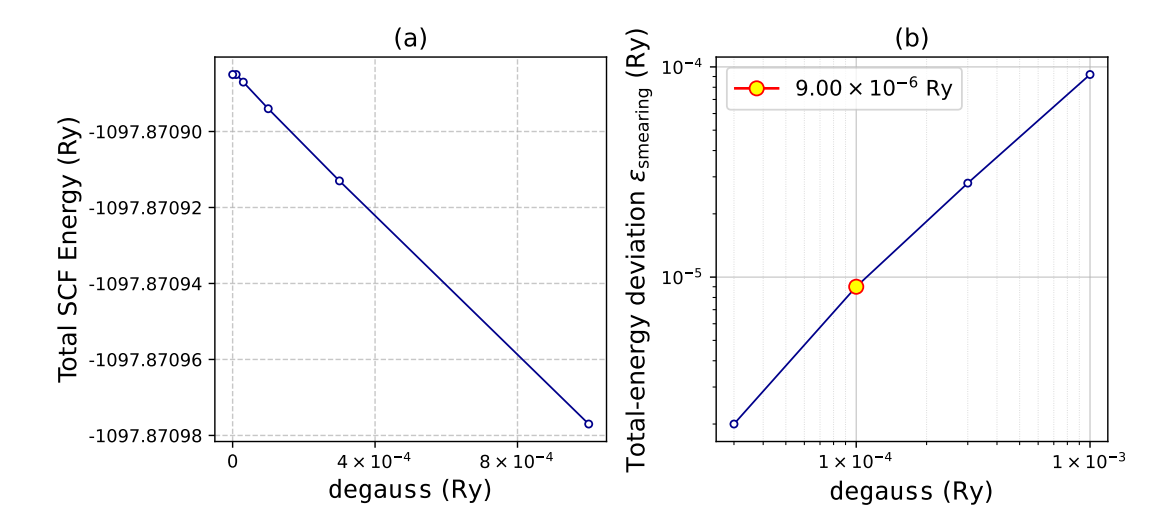


Figure 3.5: (a): the total SCF energy estimation of a 0.42 nm (12, 0) Cu/CNT as a function of the smearing degauss. (b): the SCF energy precision for each degauss), obtained by taking the  $10^{-6}$  Ry-smearing calculation as a reference.

#### 3.3 CNT structural relaxation

The pristine tube needs to be relaxed to obtain a fully relaxed configuration. We perform the relaxation in vc-relax mode, where both ions and cell parameters are free to change. To check the convergence of the relaxation, three parameters are monitored at each step:

- Total energy difference: The change in total energy between steps should fall below  $10^{-4}$  Ry.
- Maximum force: The largest force acting on any atom should be less than  $10^{-4}$  Ry/Bohr.
- Pressure: The pressure should be less than 0.2 kbar.

Convergence is considered achieved when all these criteria are satisfied, ensuring that the relaxed structure is close to the true minimum of the potential energy surface, with negligible residual forces and stress.

The obtained unitary cell is the starting point of the simulation. Comparing identical bonds around the tube the precision is at Fermi scale. The singular elementary cell will be doubled to have a bigger hypercell to accommodate the copper atom avoiding self-interactions.

Simulation difficulties The hardware bottleneck encountered in running simulations is the RAM usage. On high-memory nodes, parallel execution of QE simulations is efficient, with computational resources allocated to balance accuracy and runtime. Luckily big-memory nodes are usually available on *Indaco*, and the queue system works well. However, the 5-days wall-time limit sometimes requires a job restart. A restart is handled smoothly by the QE restart capabilities, but of course it pays the price of a significant amount of wasted computing resources.

## Chapter 4

# Characterizing the Cu/CNT system

Our work core is to identify the energetically most favourable adsorption site for Cu adatom on CNT (12,0). From purely geometrical considerations, as anticipated in the Introduction, we identify eight non-equivalent adsorption positions for the Cu adatom, namely: T, B1 (axial bridge), B2 (oblique bridge), and H, differentiating between internal (int) and external (ext) adsorption, see Fig. 1.5.

In addition to them, for the sake of checking the effect of geometrical distortions of the tube, we consider a Cu adatom initially randomly positioned with respect to the C-network, both internally and externally. Throughout a structural relaxation, it is likely to lead toward the most stable site. Our data are gathered in Tab. 4.1.

The physical quantity we need to estimate is the adsorption energy  $E_{\rm ads}$ , which we evaluate as a difference between total adiabatic potential energies, as follows:

$$E_{\rm ads} = E_{\rm Cu/CNT} - (E_{\rm Cu} + E_{\rm CNT}). \tag{4.1}$$

Here  $E_{\rm Cu/CNT}$  is the adiabatic potential energy of the fully relaxed Cu+CNT system at the local adsorption minimum: this quantity depends on the relative position of the Cu atom with respect to the CNT, and accounts also for the structural relaxation of the CNT itself.  $E_{\rm Cu}$  is the adiabatic potential energy of a single isolated atom of copper.  $E_{\rm CNT}$  is the adiabatic potential energy of the fully relaxed CNT, without any Cu adatom. These 3 energies are evaluated in exactly the same simulation cell, with exactly the same basis set and other simulation parameters, to prevent systematic errors.

In the following sections we report the methodology and simulations leading to the data reported in Tab. 4.1 for the adsorption of a Cu atom on a (12,0)

Site	$E_{ m ads} \; ({ m eV})$	$\bar{d}_{ ext{Cu-C}}  ext{ (pm)}$
ext-T	→ B1	
ext-B1	-0.61	213
ext-B2	-0.50	215
ext-H	-0.30	231
int-T	-0.13	213
int-B1	-0.12	221
int-B2	-0.13	228
int-H	-0.10	244

Table 4.1: Adsorption energy  $E_{\text{ads}}$  in eV, and average distance  $d_{\text{Cu-C}}$  between Cu and the nearest neighboring C-atoms, for external (top) and internal (bottom) adsorption.

CNT.

## 4.1 External adsorption

We find the ext-T site to be unstable. As illustrated in Fig. 4.1(a), we place initially the Cu atom directly above a C-atom, and we relax the system. The adatom moves reaching the ext-B2 position, Fig. 4.1(c). To further confirm the instability of the T-position, we start a new relaxation placing Cu slightly tilted toward the hexagon center, Fig. 4.1(b). The final result is the same, confirming the top site instability towards the neighboring axial bridge (B1) site. The stability of the ext-B1-site is confirmed by another independent random search, starting with Cu placed randomly in the vicinity of the CNT surface between all the sites.

The ext-B2 site, see Fig. 4.2, geometrically not equivalent to ext-B1 due to the tube's curvature, is also a locally stable adsorption site, which exhibits a different adsorption energy. As reported in Tab. 4.1, ext-B2 is less stable than ext-B1, with a relatively small but significant energy difference exceeding 100 meV.

The hollow site, see Fig. 4.3, is also a stable adatom position, but its binding energy lies significantly (approximately 300 meV) above B1.

## 4.2 Internal adsorption

The main novelty of the internal adsorption sites is that they are all stable local minima (including the int-T site depicted in Fig. 4.4), with quite similar ad-

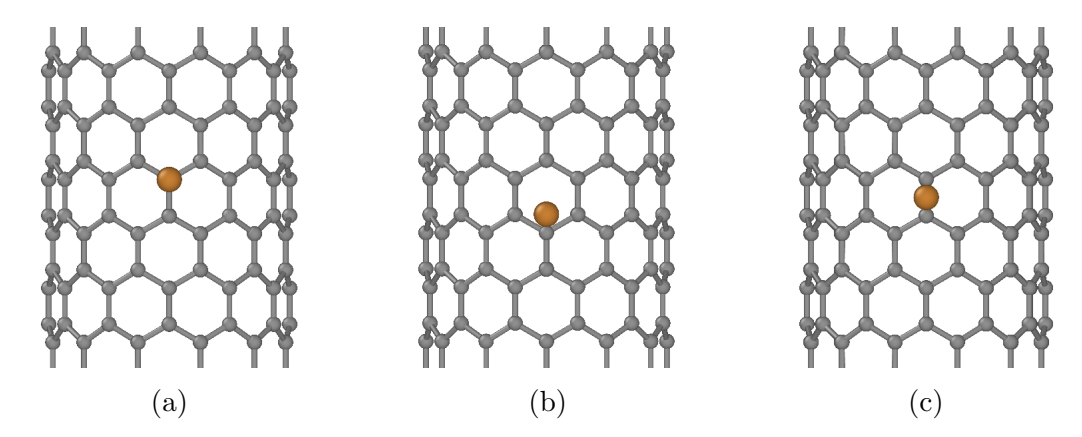


Figure 4.1: (a) and (b): Initial configurations for Cu on a (12,0) CNT. (a) is an ext-T position; (b) is near an ext-T slightly tilted toward the hexagon center. (c) The final int-B1 relaxed structure obtained at the end of both relaxations starting from the unstable initial configurations of panels (a) and (b).

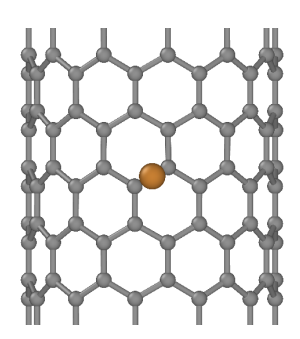


Figure 4.2: ext-B2 adsorbed Cu, relaxed structure from the simulations

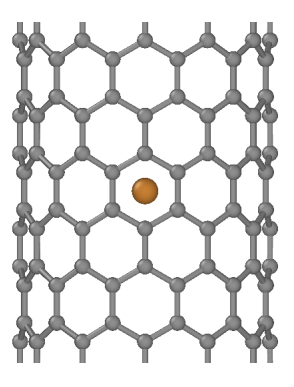


Figure 4.3: Relaxed external hollow (ext-H) site for Cu on a (12,0) CNT.

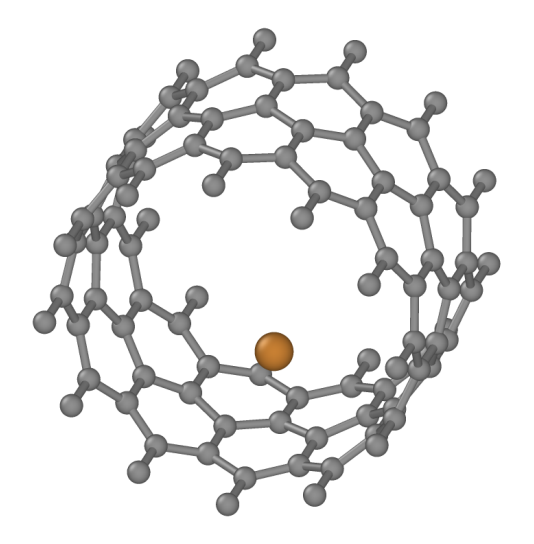


Figure 4.4: Relaxed int-T Cu adsorption on CNT (12, 0). Even though the ext-T site is unstable, the int-T site is a proper local minimum of the adiabatic potential, thus we predict it to be a valid adsorption site. In practice, this site has nearly the same adsorption energy as the other internal sites.

sorption energies. This observation hints at a much flatter inside lateral energy landscape than when the adatom threads the CNT at the outside.

Binding energies are much lower than the corresponding ones for the external sites. It seems that the curvature pushes a significant fraction of the carbon  $\pi$  orbitals outside the CNT, thus decreasing the amount of electrons available to create bonds with copper in the internal region.

## 4.3 Structural analysis

Curvature also affects the equilibrium distances between the Cu atom and the neighboring C-atoms on the CNT surface. We observe a larger distance in the internal sites, associated to weaker bonding energy, as reported in Tab. 4.1.

In addition to the Cu-C bonding distance, it is also interesting to examine the deformations of the CNT upon Cu adsorption. For this purpose, we conduct a geometrical analysis of the relaxed Cu/CNT compared to the pristine CNT.

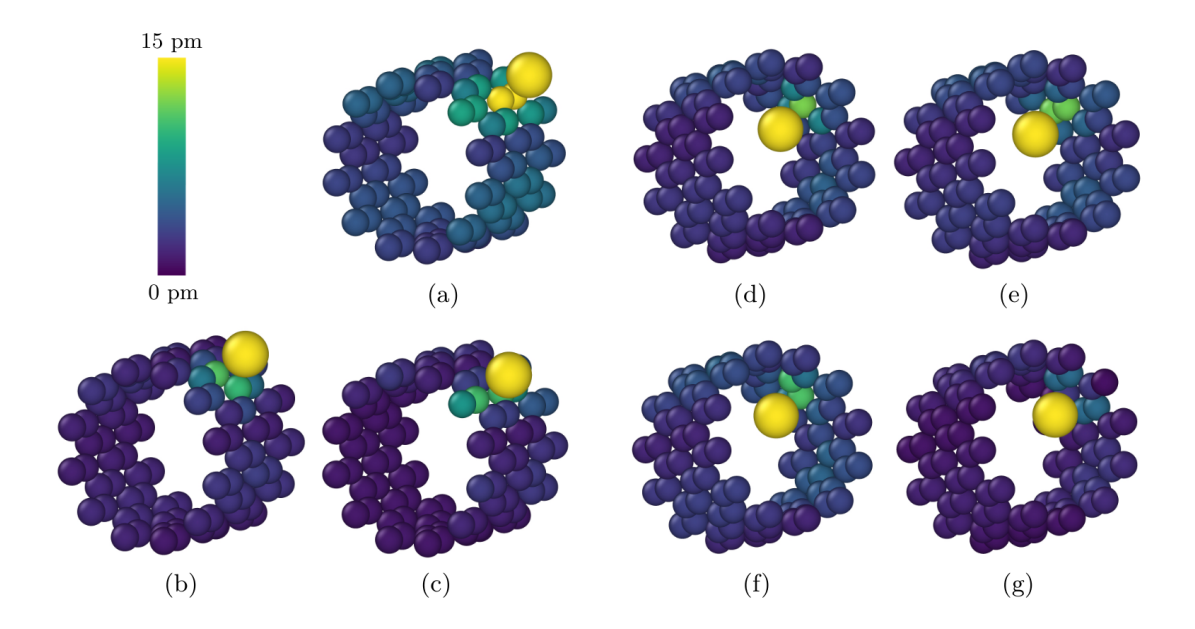


Figure 4.5: Total atomic displacement, TAD, of each C-atom after Cu adsorption at various sites, both externally and internally to the tube. Atoms are colored accordingly to their TAD using the color map. (a) ext-B1; (b) ext-B2; (c) ext-H; (d) int-T; (e) int-B1; (f) int-B2; (g) int-H.

### 4.3.1 Total atomic displacement

To illustrate how the CNT deforms to accommodate the Cu atom, we estimate the total atomic displacement of each C-atom, defined as the difference between its position before and after Cu-adsorption. Figure 4.5 reports the color map of the total atomic displacement, TAD.

Displacement vectors are computed with respect to the initial configuration of the relax calculation. We follow the common practice to correct the final configuration by fixing the center of mass of the C atoms, ensuring a consistent and translation-invariant definition of the molecular structure.

In most of the seven cases, only atoms near the adsorption site are displaced. Minor changes are observed all over the CNT, showing that the whole structure is affected by Cu adsorption, see Fig. 4.5. This global deformation is probably an artifact of the periodically repeated Cu along the CNT axis, a finite "Cu doping" with a linear density of Cu atoms amounting to 0.12 nm<sup>-1</sup>.

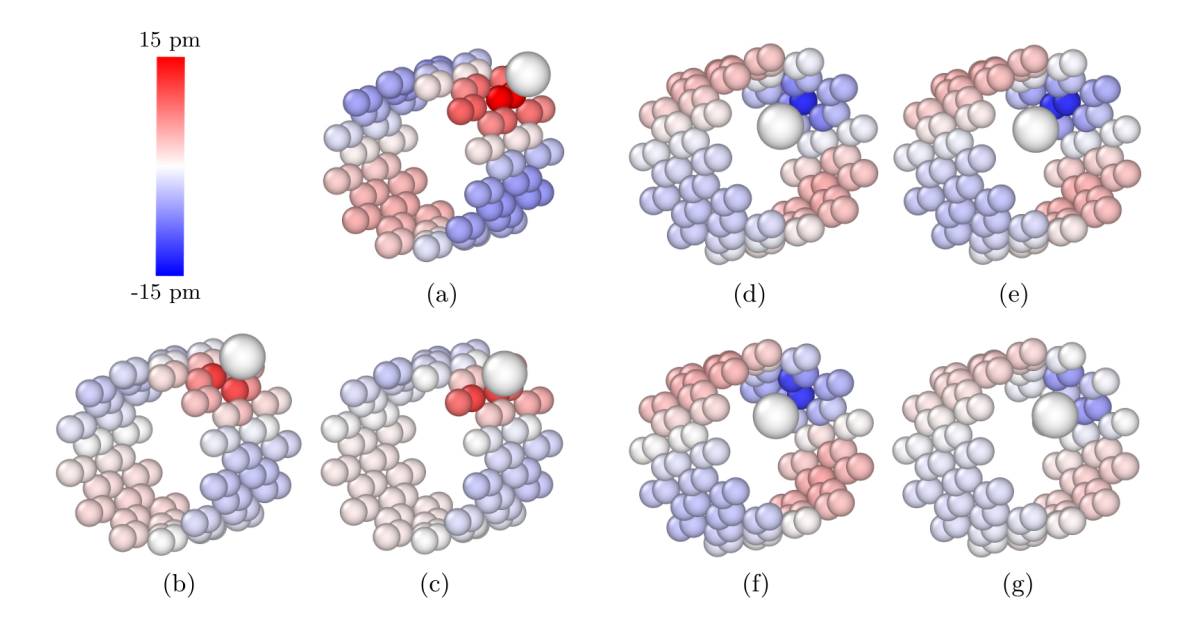


Figure 4.6: Radial deformation of CNT induced by Cu sitting at various adsorption sites. Atoms are colored according to the color map. Positive values (blue) indicate radial expansion, while negative (red) values refer to compression. This figure does not consider the Cu atom displacement. (a) ext-B1; (b) ext-B2; (c) ext-H; (d) int-T; (e) int-B1; (f) int-B2; (g) int-H.

### 4.3.2 Radial deformation

Figure 4.6 shows a color map of the radial displacement of the CNT upon Cu adsorption. The radial displacement for each C atom is defined as

$$\Delta r = \sqrt{x^2 + y^2} - \sqrt{x_0^2 + y_0^2}, \qquad (4.2)$$

where x and y are the final coordinates perpendicular to the tube axis, and  $x_0$  and  $y_0$  are those of the pristine CNT. As in the previous section 4.3.1, the final coordinates are translated to match the same center of mass of the C-atoms.

By examining the radial deformation induced by the metal adsorbate, we note that when Cu adsorbs externally, the C-atoms at the adsorption site are expanded, and so are their diametrically opposed counterparts. Conversely, a contraction is observed at the "lateral" C-sites, but milder for oblique bridge-adsorption and hollow. On the other hand, as expected, internal adsorption leads to a radial contraction of the C-atoms near Cu and on opposite to the adsorption site, accompanied by a slight expansion of the remaining C-atoms. We note that

$$\begin{pmatrix} -0.45 & 0.02 & -0.04 \\ -0.45 & 0.01 \\ 1.99 \end{pmatrix} \begin{pmatrix} -0.51 & 0.03 & -0.01 \\ -0.49 & 0.02 \\ 1.56 \end{pmatrix} \begin{pmatrix} -0.47 & 0.06 & 0.00 \\ -0.47 & 0.00 \\ 1.46 \end{pmatrix}$$
 ext-B1 ext-B2 ext-H 
$$\begin{pmatrix} -0.45 & -0.05 & -0.01 \\ -0.45 & -0.01 \\ 1.25 \end{pmatrix} \begin{pmatrix} -0.45 & -0.04 & 0.00 \\ -0.45 & 0.00 \\ 1.43 \end{pmatrix} \begin{pmatrix} -0.45 & -0.03 & 0.00 \\ -0.46 & 0.00 \\ 1.26 \end{pmatrix}$$
 int-B1 int-B2 
$$\begin{pmatrix} -0.45 & -0.03 & 0.00 \\ -0.45 & 0.00 \\ 1.52 \end{pmatrix}$$
 int-H

Table 4.2: Stress tensors in kbar computed via QE scf simulations from the relaxed Cu+CNT structures of all adsorption sites.

the radial deformation from internal adsorption is similar for top and bridge sites, but weaker for hollow. This ovalization effect has been identified in other works [26].

#### 4.3.3 Stress tensor

We estimate the stress tensor evaluated at the end of QE simulations for Cu+CNT. We conduct all the simulations with a non-variable cell obtained from the pristine tube calculations, see Fig. 4.2.

Compared to the pristine tube (see Tab. 3.1), the zz axial component increases up to  $\sim 2$  kbar for certain adsorption sites, indicating that the CNT structure tends to elongate slightly to accommodate the adatom.

Tiny off-diagonal shear components appear in the tensor. The interaction between the cell-asymmetric Cu and other periodic images of the CNT in the x and y directions is responsible for the xy component. The xz and yz components represent shear stress on the simulation-box faces that glue together the periodic CNT image sections.

In a real scenario with a long CNT, the z components of the stress tensor would be relieved through likely asymmetric local expansion of the CNT around

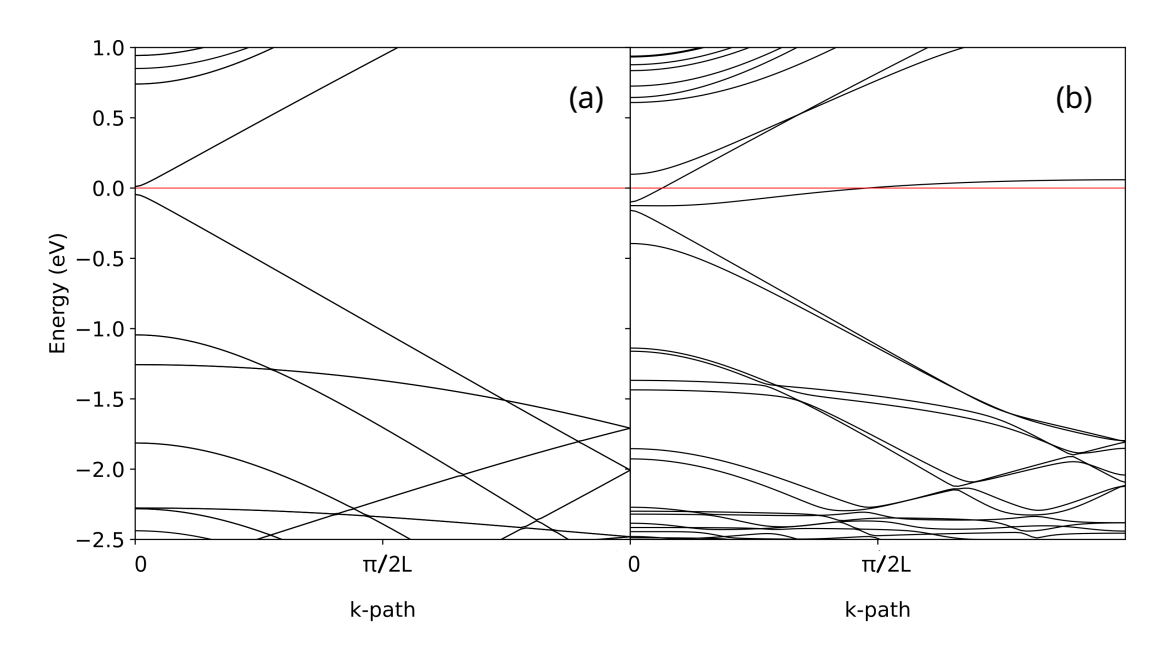


Figure 4.7: Electronic bands comparison between pristine CNT (a) and Cu/CNT ext-B1 adsorbate (b). Fermi level is set at 0 eV. L represent the z axis length of the simulation cell.

the adatom, which will lead to a little bending of the CNT. The other components are non-physical and do not correspond to any actual structural adaptation of the tube to the adsorption of Cu.

## 4.4 Electronic structure and charge analysis

To explore the effect of Cu adsorption on the electronic nature of the CNT, we examine the band structure and charge distribution of both pristine and Cudecorated CNTs. Band structure calculations are carried out to identify modifications in the electronic states induced by Cu. In addition, we use Bader charge
analysis to quantify charge transfer between the Cu atom and the CNT. The
results reveal that Cu acts as an electron donor, transferring charge to the nanotube and inducing a transition from a small-gap semiconducting behavior to a
metallic character.

#### 4.4.1 Electronic bands

We compute the band structure for the pristine CNT, which exhibits semiconducting nature with a 0.056 eV band gap, as shown in Fig. 4.7(a). Since the calcu-

Site	charge on Cu $(e)$
ext-B1	$+0.28 \pm 0.05$
ext-B2	$+0.28 \pm 0.05$
ext-H	$+0.34 \pm 0.05$
int-T	$+0.26 \pm 0.05$
int-B1	$+0.26 \pm 0.05$
int-B2	$+0.26 \pm 0.05$
int-H	$+0.29 \pm 0.05$

Table 4.3: Cu-valence charge difference with respect to the nominal valence charge of a free atom, computed with Bader's method. Software provided by *Henkelman Research Group* [9, 20, 23, 2].

lations are performed in a duplicated minimal cell, the band folding phenomenon can be observed at  $k_z = \pi/L$ , in particular in two filled bands of Fig. 4.7(a). All the bands exhibit a double degeneracy arising from the presence of additional spatial symmetries besides the translational symmetry. Upon the introduction of a single (periodically repeated) Cu atom adsorbed on the CNT, significant modifications in the electronic structure are observed. Notably, the DFT calculations reveal the emergence of a Cu-derived electronic band near the Fermi level, as displayed in Fig. 4.7(b). We observe a narrow dispersion for this Cu-related band, suggesting a non-trivial interaction between Cu replicas. This additional band crosses the Fermi energy, inducing metallic behavior in this system. A CNT band is injected a certain amount of electrons too, thus acquiring metallic behavior. The results indicate that the presence of the Cu atom lifts the Fermi energy, and introduces new states that affect the low-energy electronic properties of the adsorbed CNT.

In the adsorbed system, band folding is suppressed because adsorption reduces the translational symmetry, effectively doubling the size of the minimal unit cell. The degeneracy is lifted, as the presence of the Cu-atom breaks the additional symmetries.

## 4.4.2 Bader's charge analysis

In forming bonds, atoms delocalize their electrons within the whole structure to extended orbitals. This delocalization is associated to a kinetic -energy drop that makes bonding energetically favored. Once electrons are not localized on a specific atom, the remaining electronic charge on each atom can be different from

Research	Site	$E_{\rm ads} \; ({ m eV})$	$d_{\mathrm{Cu-C}}\ (\mathrm{pm})$
Hou 2023	Т	-0.23	218
	Н	-0.30	209
	В	-0.23	215
Tang 2017	Т	-0.29	206
	Н	-0.13	239
	В	-0.25	217

Table 4.4: DFT-PBE results for Cu adsoprtion on a single graphene layer, as available in the literature [10, 24].

the atomic state.

Richard Bader developed a method to partition the molecular electron density into atomic basins, defined by zero-flux surfaces in the gradient of the electron density. This approach allows one to determine the residual charge on the Cu atom, which is crucial for characterizing the nature of the bonding. The method is widely used, as it provides a consistent partitioning of the total electronic charge, ensuring charge conservation.

For that purpose, we employ the projwfc.x utility from QE to project the Kohn–Sham states onto atomic wavefunctions, thereby reconstructing the atom-projected density of states (PDOS) and extracting charge information.

We propose a Bader's analysis and projwfc.x projections to the Cu/CNT under study. Results from the former appear more reliable. The precision of the charge assignment is estimated to be around  $0.05\,e$ , as achieving an optimal grid separation was difficult with the program.

The resulting charge on the Cu adsorbate with respect to its valence value are reported in Tab. 4.3. We note that on all sites the Cu is more positive, hence, it is donating electrons to the CNT. The charge donation is similar whether Cu is external or internal,  $\sim -0.3\,e$ , but the hollow sites show a larger donation.

#### 4.4.3 Discussion

Here we discuss the energetic and structural features of the Cu-adsorption compared to graphene [24, 10], and different CNTs, for example the (8,0) [1, 26]. Indeed, the only available data from the literature regards external adsorption on (8,0) CNTs, with a greater curvature. Indeed its diameter is as small as 630 pm, compared to 950 pm of (12,0).

The two considered works on Cu-graphene, summarised in Table 4.4, referred to DFT data for Cu-adsorption on a graphene layer for top (T), bridge

Research	Best site	$E_{\mathrm{ads}} \; (\mathrm{eV})$	$d_{Cu-C}$ (pm)
Yang 2024	B1	-0.91	208.7
Aasi 2020	B1	-0.75	213
Xu 2023	B1	-0.53	NA

Table 4.5: Literature data available for Cu-adsorption on (8,0) CNT [26, 1, 25].

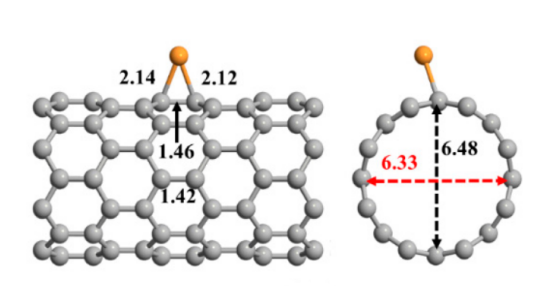


Figure 4.8: Best adsorption site for Cu on a (8,0)-CNT, lateral views. Bond lengths and diameter are shown, taken from Ref.[1]

(B), and hollow (H) sites. They employ similar DFT scheme. In particular, we note that Hou et al. results [10] employed the same functional as us, they use a smearing parameter (degauss) of 0.2 eV, while we are close to fixed occupation, and a force threshold ( $\sim 0.5$  Ry/Bohr) which might be too large. Tang et al. [24] employed spin-polarized DFT with the PBE-PAW approach. Nonetheless, both groups reports  $E_{ads}$  in the same range, although Tang predicts the top as the best site while Hou finds the hollow as the most stable. On that regard we note a considerable difference in the Cu-C distance for the H-site that might explain the difference between the calculations. For T nd B sites, the Cu-C distance is between 206-218 pm. Their results support the hypothesis that  $\pi$ -orbital rehybridization increases the electronic density at the external sites, thereby enhancing the bonding strength at these positions at the expense of the internal ones.

Aasi et al. [1] investigated the catalytic properties of metal-adsorbed (8,0) CNTs interacting with oxidant hydrogen peroxide. They show the axial bridge as the most stable for Cu on (8,0)-CNT with a binding energy of  $E_{\rm ads} = -0.75$  eV, which is considerably less than that estimated by Yang et al.[26]. Aaasi et al. report slightly asymmetric bond length of 2.14 and 2.12 of Cu bonded to the two C-atoms, see Fig. 4.8. They also note a longer C-C bonds (0.03% more) and

a longer diameter for the ring where Cu sits, 6.48 vs 6.33 Å.

We note that the average distance of Cu for the B1 adsorption,  $d_{\text{C-Cu}} = 213 \text{ pm}$ , is in perfect agreement with our value on the (12,0)-CNT. The radial deformation is in agreement with our calculations. A stronger adsorption on the (8,0) than on the (12,0) is expected because the latter has a lower curvature. More in specific, our estimate in the adsorption energy falls in between those on graphene and the (8,0)-CNT. Furthermore, the (12,0) is able to accommodate metal atoms inside the tube, suggesting a new design possibility.

### 4.5 Conclusion

Overall, our DFT calculations suggest that preferred adsorption sites are the external bridges and hollow. We find that a Cu atom can bind inside the CNT but the binding energy is as low as 0.13 eV. Nanotube curvature induced effects are the destabilization of external top site and the strong difference between internal and external bond strength.

Our results highlight the role of CNT curvature in modulating adsorption properties, and demonstrate good agreement with prior studies on similar carbon-based materials. Indeed we show that the binding energy of Cu decreases from an estimate of 0.75 eV on (8,0) to 0.61 eV on a (12,0)-CNT, although the Cu-C distance are mostly preserved.

Future work could extend these findings by exploring:

- Adsorption of multiple metals and cooperative effects.
- Functionalized CNTs to enhance binding and electronic response.
- Design of CNT-based catalysts.
- Temperature effects through ab initio molecular dynamics.
- Comparison with experimental spectroscopic and electrochemical data.

These perspectives will further clarify the potential of CNTs as platforms for catalysis, sensing, and energy storage applications.

# Appendix A

# CNT configuration generator

In this appendix we report the full code that we wrote for generating the atomic positions of an arbitrary single-wall CNT.

```
#include <cmath>
#include <iostream>
#include <fstream>
#include <vector>
#include <armadillo>
#include <string>
#include <iomanip>
#include <numeric>
// C++17 needed
using namespace std;
using namespace arma;
const double epsilon{0.00001};
int main(int argc, char** argv) {
    if (argc < 6 - (argc - 6))
        return -1;
    }
    string filename{argv[1]};
    ofstream fout(filename, ios::out);
    int n{atoi(argv[2])};
    int m{atoi(argv[3])};
    int repetitions{atoi(argv[4])};
    double a{atof(argv[5])};
    int NExotics{(argc - 6) / 4};
    vector<string> exoticNames(NExotics);
    vector<vec> exoticIndexes(NExotics);
```

```
vector<double> exoticDistances(NExotics);
for (int i{}; i < NExotics; i++) {</pre>
    exoticNames[i] = string(argv[6 + 4*i]);
    exoticIndexes[i] = vec({
        atof(argv[6 + 4*i + 1]),
        atof(argv[6 + 4*i + 2])
    });
    exoticDistances[i] = atof(argv[6 + 4*i + 3]);
}
vector<vec> points(0);
vec a1 = \{1., 0.\};
vec a2 = \{0.5, sqrt(3.) / 2.\};
vec b((a1 + a2) * 2. / 3.);
int nc\{-(n + 2*m) / gcd(n+2*m, m+2*n) * repetitions\};
int mc\{(m + 2*n) / gcd(n+2*m, m+2*m) * repetitions\};
vec A = n * a1 + m * a2;
double A2{arma::dot(A, A)};
double sqrtA2{sqrt(A2)};
cout << "Tube width = " << sqrtA2 / M_PI * a << "A" << endl;</pre>
vec C = nc * a1 + mc * a2;
double C2{arma::dot(C, C)};
double sqrtC2{sqrt(C2)};
cout << "Tube lenght = " << sqrtC2 * a << "A" << endl;</pre>
vec candidateOnGraphene(2);
vec pointOnTube(3);
int minN {min(min(0, n),
    min(nc, n + nc)),
    \max N \{\max(\max(0, n),
    \max(nc, n + nc)),
    minM {min(min(0, m),
    min(mc, m + mc)),
    maxM \{max(max(0, m),
    max(mc, m + mc));
int counter{};
double relativeProjectionA{}, relativeProjectionC{};
for (int n_i{minN}; n_i < maxN; n_i++) {</pre>
    for (int m_i{minM}; m_i < maxM; m_i++) {</pre>
        candidateOnGraphene = n_i * a1 + m_i * a2;
        relativeProjectionA = arma::dot(candidateOnGraphene, A) / A2;
```

```
relativeProjectionC = arma::dot(candidateOnGraphene, C) / C2;
        if (relativeProjectionA >= -epsilon
            && relativeProjectionA < 1 - epsilon
            && relativeProjectionC >= -epsilon
            && relativeProjectionC < 1 - epsilon) {
            relativeProjectionC += epsilon;
            pointOnTube(0) = cos(relativeProjectionA * 2. * M_PI) *
                sqrtA2 / 2. / M_PI * a;
            pointOnTube(1) = sin(relativeProjectionA * 2. * M_PI) *
                sqrtA2 / 2. / M_PI * a;
            pointOnTube(2) = (relativeProjectionC - floor(relativeProjectionC)
                - 0.5) *sqrtC2 * a;
            points.push_back(pointOnTube);
            counter++;
            candidateOnGraphene = n_i * a1 + m_i * a2 + b;
            relativeProjectionA = arma::dot(candidateOnGraphene, A) / A2;
            relativeProjectionC = arma::dot(candidateOnGraphene, C) / C2 + epsilon;
            pointOnTube(0) = cos(relativeProjectionA * 2. * M_PI) *
                sqrtA2 / 2. / M_PI * a;
            pointOnTube(1) = sin(relativeProjectionA * 2. * M_PI) *
                sqrtA2 / 2. / M_PI * a;
            pointOnTube(2) = (relativeProjectionC - floor(relativeProjectionC)
                -0.5) * sqrtC2 * a;
            points.push_back(pointOnTube);
            counter++;
        }
    }
}
cout << "Total points generated: " << counter + NExotics << endl;</pre>
fout << counter + NExotics << endl;</pre>
fout << scientific;</pre>
fout << setprecision(10);</pre>
fout << "#Width: " << sqrtA2 / M_PI * a</pre>
     << " ---Lenght: " << sqrtC2 * a << endl;
for (auto v : points) {
    fout << "C"
         << setw(20) << v(0)
         << setw(20) << v(1)
         << setw(20) << v(2)
```

```
<< endl;
    }
    for (int i{}; i < NExotics; i++) {</pre>
        candidateOnGraphene = exoticIndexes * a1 + exoticIndexes * a2;
        relativeProjectionA = arma::dot(candidateOnGraphene, A) / A2;
        relativeProjectionC = arma::dot(candidateOnGraphene, C) / C2 + epsilon;
        fout << exoticNames[i]</pre>
             << setw(20) << (cos(relativeProjectionA * 2. * M_PI)) *
             (sqrtA2 / 2. / M_PI * a + exoticDistances[i])
             << setw(20) << (sin(relativeProjectionA * 2. * M_PI)) *
             (sqrtA2 / 2. / M_PI * a + exoticDistances[i])
             << setw(20) << (relativeProjectionC - floor(relativeProjectionC)</pre>
             - 0.5) * sqrtC2 * a
             << endl;
    }
    fout.close();
    return 0;
}
```

# **Bibliography**

- [1] A. Aasi, S. M. Aghaei, M. D. Moore, and B. Panchapakesan. Pt-, rh-, ru-, and cu-single-wall carbon nanotubes are exceptional candidates for design of anti-viral surfaces: A theoretical study. *International Journal of Molecular Sciences*, 21(15):5211, 2020.
- [2] R. F. W. Bader. Bader charge analysis code. http://theory.cm.utexas.edu/bader/. Accessed 2025-10-15.
- [3] D. S. Bethune, C. H. Kiang, M. S. de Vries, G. Gorman, R. Savoy, J. Vazquez, and R. Beyers. Cobalt-catalysed growth of carbon nanotubes with single-atomic-layer walls. *Nature*, 363:605–607, 1993.
- [4] S. Dorfman, D. Fuks, and D. E. Ellis. Formation of nano-crystalline structure at the interface in cu–c composite. *Applied Surface Science*, 94:431–436, 1996.
- [5] J. O. L. Fuentes. Co<sub>2</sub> absorption on cu-doped graphene, a dft study. *Crystals*, 15(5):460, 2025.
- [6] P. Giannozzi, O. Andreussi, T. Brumme, O. Bunau, M. Buongiorno Nardelli, M. Calandra, R. Car, C. Cavazzoni, D. Ceresoli, M. Cococcioni, N. Colonna, I. Carnimeo, A. Dal Corso, S. de Gironcoli, P. Delugas, R. A. DiStasio Jr, A. Ferretti, A. Floris, G. Fratesi, G. Fugallo, R. Gebauer, U. Gerstmann, F. Giustino, T. Gorni, J. Jia, M. Kawamura, H.-Y. Ko, A. Kokalj, E. Küçükbenli, M. Lazzeri, M. Marsili, N. Marzari, F. Mauri, N. L. Nguyen, H.-V. Nguyen, A. Otero de-la Roza, L. Paulatto, S. Poncé, D. Rocca, R. Sabatini, B. Santra, M. Schlipf, A. P. Seitsonen, A. Smogunov, I. Timrov, T. Thonhauser, P. Umari, N. Vast, X. Wu, and S. Baroni. Advanced capabilities for materials modelling with quantum espresso. Journal of Physics: Condensed Matter, 29:465901, 2017.
- [7] P. Giannozzi, S. Baroni, N. Bonini, M. Calandra, R. Car, C. Cavazzoni, D. Ceresoli, G. L. Chiarotti, M. Cococcioni, I. Dabo, A. Dal Corso, S. Fab-

- ris, G. Fratesi, S. de Gironcoli, R. Gebauer, U. Gerstmann, C. Gougoussis, A. Kokalj, M. Lazzeri, L. Martin-Samos, N. Marzari, F. Mauri, R. Mazzarello, S. Paolini, A. Pasquarello, L. Paulatto, C. Sbraccia, S. Scandolo, G. Sclauzero, A. P. Seitsonen, A. Smogunov, P. Umari, and R. M. Wentzcovitch. Quantum espresso: a modular and open-source software project for quantum simulations of materials. *Journal of Physics: Condensed Matter*, 21(39):395502, 2009.
- [8] P. Giannozzi, O. Baseggio, P. Bonfà, D. Brunato, R. Car, I. Carnimeo, C. Cavazzoni, S. de Gironcoli, P. Delugas, F. Ferrari Ruffino, A. Ferretti, N. Marzari, I. Timrov, A. Urru, and S. Baroni. Quantum espresso toward the exascale. The Journal of Chemical Physics, 152:154105, 2020.
- [9] G. Henkelman, A. Arnaldsson, and H. Jónsson. A fast and robust algorithm for bader decomposition of charge density. *Computational Materials Science*, 36(3):354–360, 2006.
- [10] Huinan Hou, Vignesh Murugadoss, Zhuofan Qin, Ding Wang, Yifan Li, and Ben Bin Xu. Mechanical properties of graphene-metal composite system: a first principles study. *Advanced Composites and Hybrid Materials*, 6(3):1–9, 2023.
- [11] S. Iijima. Helical microtubules of graphitic carbon. *Nature*, 354(6348):56–58, 1991.
- [12] S. Iijima and T. Ichihashi. Single-shell carbon nanotubes of 1-nm diameter. Nature, 363:603–605, 1993.
- [13] Abida Jan, Midhat Batool, Surya Nath Pandey, Muhammad Afzal, Ahsas Goyal, and Mohd Imran Ansari. Functionalized graphene quantum dots (fgqds): A review of their synthesis, properties, and emerging biomedical applications. *Carbon Trends*, 18:100442, 2024.
- [14] A. Kleiner and S. Eggert. Curvature, hybridization, and stm images of carbon nanotubes. *Physical Review B*, 64:113402, 2001.
- [15] Tadahiro Komeda. Comparison of stm images of armchair and zigzag carbon nanotubes. Figure uploaded on ResearchGate, 2004. Upper panel: interference pattern near the end-cap of armchair-like semiconducting CNT (chiral vector (28, -13)),  $I_t = 100$  pA,  $V_{bias} = 0.6$  V. Content may be subject to copyright.

- [16] Yang Liu, Zefei Wu, Chen Gu, Jianmei Chen, Yanwei Zhu, and Longlu Wang. Curved structure regulated single metal sites for advanced electrocatalytic reactions. *Small*, 20(47):e2404758, 2024.
- [17] Nicola Manini. Introduction to the Physics of Matter: Basic Atomic, Molecular, and Solid-State Physics. Undergraduate Lecture Notes in Physics. Springer International Publishing, 2 edition, 2020. Print ISBN: 9783319143811.
- [18] W. O. Morais, J. P. C. Felix, and G. R. D. Silva. Understanding stability and reactivity of transition metal single-atoms on graphene. *Scientific Reports*, 15:15496, 2025.
- [19] D. Perilli, S. M. Alayoglu, J. L. G. Fierro, S. M. S. M., J. L. G. Fierro, and S. M. S. M. Co adsorption on a single-atom catalyst stably confined in graphene on ni(111). *Angewandte Chemie International Edition*, 64(4):1234–1237, 2025.
- [20] Edward Sanville, Steven D. Kenny, Roger Smith, and Graeme Henkelman. An improved grid-based algorithm for bader charge allocation. *Journal of Computational Chemistry*, 28(5):899–908, 2007.
- [21] David F. Shanno. Conditioning of quasi-newton methods for function minimization. *Mathematics of Computation*, 24(111):647–656, 1970.
- [22] M. A. Stoodley, L. A. Rochford, T.-L. Lee, B. P. Klein, D. A. Duncan, and R. J. Maurer. Structure of graphene grown on cu(111): X-ray standing wave measurement and density functional theory prediction. *Physical Review Letters*, 132(19):196201, 2024.
- [23] Wenjie Tang, Edward Sanville, and Graeme Henkelman. A grid-based bader analysis algorithm without lattice bias. *Journal of Physics: Condensed Mat*ter, 21(8):084204, 2009.
- [24] Yanan Tang, Hongwei Zhang, Zigang Shen, Mingyu Zhao, Yi Li, and Xianqi Dai. The electronic and diffusion properties of metal adatoms on graphene sheets: a first-principles study. *RSC Advances*, 7:33208–33218, 2017.
- [25] LeLe Xu, XinYu Jiao, Chao Shi, An-Ping Wu, Peng-Xiang Hou, Chang Liu, and Hui-Ming Cheng. Single-walled carbon nanotube/copper core—shell fibers with a high specific electrical conductivity. ACS Nano, 17:9245—9254, 2023.

[26] J. Yang. Density functional theory study of adsorption and doping of transition metal atoms on carbon nanotube surfaces. *Carbon Trends*, 8:100292, 2024.